## 6.1 Introduction

Catalytic activities of nanoparticles are a function of their size, shape, composition and nanostructure [Cao *et al.* (2016), Mclaren *et al.* (2009)]. The composition of nanoparticles can be varied by preparing their alloy/bimetallics. Physicochemical properties of bimetallic nanoparticles are sensitive to composition, spatial arrangement and atomic ordering of the different types of atoms. In conjunction with this, the nanostructure formed is also very important. Thus, different bimetallic nanostructures, instead of simple monometallic nanocrystals, can give improved catalytic properties and also create a new property, which may not be achieved by individual component monometallic catalysts [Wu *et al*. (2012), Zhang *et al*. (2011), Yin *et al*. (2011), Yoo *et al.* (2011), Sun *et al*. (2009)]. Therefore, a large number of synthetic protocols have been established that are capable of producing a broad range of bimetallic nanocrystal with well-defined atomic-scale features such as faceting, atomic ordering, and spatial arrangement. Bimetallic nanomaterials include alloys, core shell and core frame structures [Gilroy *et al.* (2016), Toshima and Yonezawa (1998)].

The novel optical properties are associated with bimetallic nanomaterials, facilitated innovative applications, which are related to sensing, imaging, catalysis, along with plasmonically enhanced chemistry, spectroscopy, and light harvesting [Kim *et al.* (2014), Xiao *et al.* (2014a), Xiao *et al.* (2014b), Wang *et al.* (2013)]. Alloying or forming bimetallic nanoparticles (NPs) of cheaper elements with precious metals not only make them use cost effective but also modify the mechanism of chemical reactions on solid surfaces. Due to synergistic effects, many bimetallic NPs exhibit improved catalytic, optical, electronic, and magnetic properties [Zhang *et al.* (2015a), Zhang *et al.* (2015b), Wang *et al.* (2008)] better

than the elements constituting the nanoparticles. Besides composition and size, the nature of nanostructures, such as cluster-in-cluster, core-shell, Janus nanoparticles and random alloys also affects the catalytic activity of these nanoparticles.

Bimetallic nanoparticles like Ag-Ni, Ag-Pd, Au-Cu, Pt-Ni, Ag-Cu, etc. [Wu *et al.* (2015), Kumar and Deka (2014), He *et al.*(2014b), Li *et al.* (2013), Ghosh *et al.* (2004)] have been used as catalysts for the conventional Nip reduction by $NaBH_4$. For instance, authors [Kumar and Deka (2014)] reported that $Ag_{1-x}Ni_x$ alloy NPs as a catalyst for Nip reduction by $NaBH_4$ shows synergistic activity at certain combinations of composition and nanostructure. Likewise, there are other reports in literature as well of similar results [Wu *et al.* (2015)] on conventional Nip reduction by $NaBH_4$. However studies on the effect of composition and nanostructure of bimetallic nanoparticles on their catalytic activities for Nip reduction by glycerol seem to be lacking in literature. Naturally, in an effort to reduce the cost of the catalyst, in the present work the effect of using Ag-Cu bimetallic nanoparticles are investigated as catalysts for Nip reduction with i) $NaBH_4$ and ii) glycerol (Gly). Further the oxidative degradation of methyl orange (MO) in presence of these bimetallic nanoparticles is also studied.

As the Ag-Cu equilibrium phase diagram displays extremely low level of solid solubility at ambient temperature. Thus, solid solution formation in silver and copper rich side of phase diagram will be possible only under metastable condition. Besides this, there is also the problem of the large difference between reduction potentials of Ag (~ 0.80 eV) and Cu (~ 0.34 eV). Consequently, both are not reduced at the same rate leading to formation of bimetallic nanostructures in the Ag-Cu system. Therefore, this chapter deals with the synthesis of Ag-Cu bimetallic nanomaterials with three different variations. First is the

synthesis of Ag-Cu BNPs by a polyol protocol and the effect of precursor salts composition on the shape and size of bimetallic nanoparticles. Second, Ag core Cu shell (Ag@Cu) and Ag shell Cu core (Cu@Ag) structures are produced with the same polyol synthesis protocol. In the third variation, initially prepared Cu seed nanoparticles, $Ag(NH_3)_2^+$ solution (which is more stable towards reduction as compared to $Ag^+$) and precursor $Cu^{2+}$ salt were co-reduced by a strong reducing agent. Prepared bimetallic nanoparticles were then utilized as catalysts for Nip reduction and MO oxidation. In view of the good plasmonic photocatalytic properties of Ag and Cu nanoparticles (Chapters-3, 4 and 5), Nip reduction (by Gly) and MO oxidative degradation are also carried out under visible light. Photocatalytic enhancement (if any) is reported. The effect of size, composition and nanostructure of the prepared Ag-Cu BNPs on the kinetics of reduction and oxidation reaction are discussed. Effect of temperature on the reaction and thereby on activation energies is also discussed.

This Chapter is divided into three major sections or parts. The first part is about the preparation of Ag-Cu BNPs by polyol method and catalytic studies using them. The second part deals with the synthesis of core-shell Ag-Cu BNPs also by polyol method and then their catalytic properties. The last part is about preparation of finer phase-separated Ag-Cu bimetallic nanoparticles in aqueous medium using a stronger reducing agent and a different protocol.

## 6.2 Catalytic studies of Ag-Cu BNPs prepared by polyol method

### 6.2.1 Experimental details

#### 6.2.1.1 Synthesis of Ag-Cu bimetallic nanoparticles

Materials used for the synthesis of Ag-Cu BNPs were $AgNO_3$ (Merck), $(CH_3COO)_2Cu.7H_2O$ (Merck), Ethylene glycol (Merck) and polyvinylpyrrolidone (PVP)

(Himedia). All reagents used were of analytical reagent grade and used without further purification. The synthesis of CuNPs, Ag-Cu BNPs and AgNPs corresponding to three (precursor salt) [Cu]/[Ag]molar ratios for Cu (1 : 0), Ag-Cu BNPs (1 : 1, 1 : 2 and 1 : 4) and for Ag (0 : 1) were attempted. For 1 : 1 (Cu : Ag) molar ratio (denoted as S2 Ag-Cu BNPs), 25 mL 0.015 M $Ag(NO_3)$, 25 mL 0.015 M $(CH_3COO)_2Cu.H_2O$ and 25 mL 0.48 M PVP (in terms of monomer unit) solutions in ethylene glycol (EG) were prepared. These solutions were then mixed in a 100 mL two necked flask and $N_2$ gas was bubbled at room temperature for about 30 minutes to remove oxygen dissolved in the solution. The reaction mixture was then kept in preheated oil bath at 443 ± 5 K under $N_2$ bubbling for 30 minutes. The precipitate formed was separated out by centrifuging at 15000 rpm. Further, the precipitate was repeatedly washed with ethanol and then dried in vacuum oven at 50 $^0$C. The same procedure was repeated to prepare nanoparticles when precursors were taken in 1 : 2 and 1 : 4 ([Cu]/[Ag]) molar ratios (hereafter denoted by sample S3 and S4 Ag-Cu BNPs respectively). To ensure proper comparison of catalytic activities and understanding of their variation with composition of nanoparticles, the same protocol was used to prepare pure PVP stabilized CuNPs and AgNPs nanoparticles. The pure PVP stabilized Cu and Ag nanoparticles are denoted by S1 and S5 respectively. Please note that sample S5 (in this chapter) and C0 (in Chapter-3) are the same.

### 6.2.2 Catalytic reduction and oxidation

#### 6.2.2.1 Catalytic Nip reduction with $NaBH_4$

The experimental details for the Nip reduction with $NaBH_4$ in presence of pure Cu, Ag and their Ag-Cu BNPs is identical to the protocol described in sub-section 3.2.2.1 of Chapter-3. The catalyst is taken as 1 mL of the prepared Ag-Cu BNPs sol was diluted by 3

times with adequate amount of water. 50 μL of the diluted Ag-Cu BNPs sol was added to the reaction mixture for its catalytic study.

#### 6.2.2.2 Catalytic Nip reduction with glycerol

The particulars of experiments for the Nip reduction with Gly as reductant in presence of pure Cu, Ag and their Ag-Cu BNPs as catalyst is identical to the protocol described in sub-section 3.2.2.2 of Chapter-3.

#### 6.2.2.3 Catalytic oxidation of MO dye

The experimental details for the oxidative MO degradation with $H_2O_2$ in presence of pure Cu, Ag and their Ag-Cu BNPs are identical to the protocol described in sub-section 3.2.2.3 of Chapter-3.

### 6.2.3 Visible light enhancement of catalytic reduction and oxidation activites

Photocatalytic activity is measured by placing the reaction mixtures in photocatalytic chamber as described in Chapter-2. The temperature of the photocatalytic chamber was measured to be 306 K.

#### 6.2.3.1 Photocatalytic enhancement of Nip reduction with glycerol

The reaction mixture with pure Cu, Ag and their Ag-Cu BNPs catalyst was prepared as given in section 3.2.2.2, this is then irradiated by visible light from cool white LED source (approximately 940 watts/$m^2$) in the photocatalytic chamber at 306 K.

#### 6.2.3.2 Photocatalytic oxidation of methyl orange dye

The reaction mixture with the catalyst was prepared as given in section 3.2.2.3. The reaction mixture was kept in the photocatalytic chamber at 306 K and then irradiated by

visible light from cool white LED source (approximately 940 watts/$m^2$). The kinetics and photocatalytic activities were measured for pure Cu, Ag and Ag-Cu BNPs catalysts samples.

### 6.2.4. Results and discussion

#### 6.2.4.1 Characterization of Ag-Cu bimetallic nanoparticles

X-ray diffraction patterns of the nanoparticle powder samples S1, S2, S3, S4 and S5 are shown in Figure 6.2.1. S1 CuNPs sample shows three peaks at 43.23, 51.02 and 74.13 corresponding to {111}, {200} and {220} planes of FCC copper and Sample S5 AgNPs shows four peaks at 38.18°, 44.40°, 64.66° and 77.07° corresponding to the {111}, {200}, {220} and {311} of FCC silver.

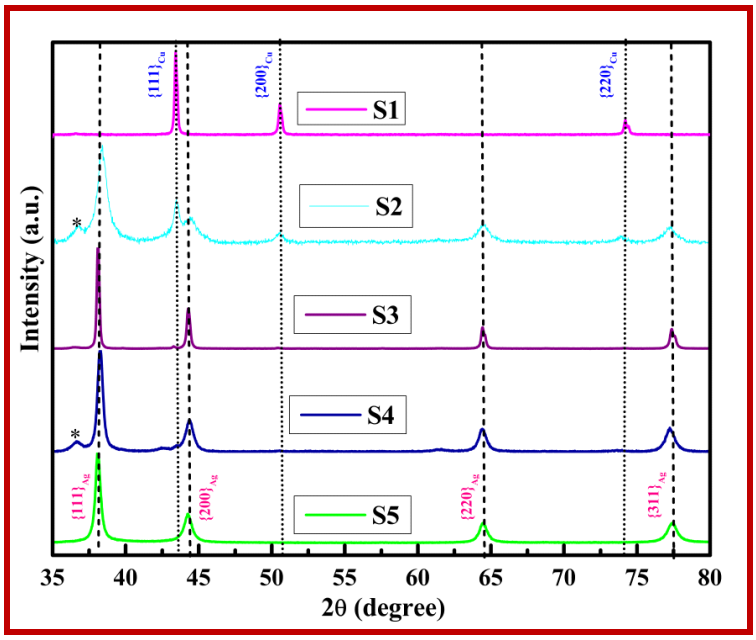


**Figure 6.2.1** X-ray powder diffraction patterns of S1, S2, S3, S4and S5 samples.

Further, in Sample S2 Ag-Cu BNPs four peaks were observed at 38.18°, 44.40°, 64.66° and 77.07° corresponding to the {111}, {200}, {220} and {311} planes of FCC silver and three peaks at 43.24°, 51.04° and 74.13° corresponding to {111}, {200} and {220}

planes of FCC copper. For S3 and S4 Ag-Cu BNPs samples with the presence of four peaks at 38.17°, 44.42°, 64.63° and 77.09° corresponding to the {111}, {200}, {220} and {311} planes of FCC silver one peak at 38.19° corresponding to {111} plane of copper is observed. Thus, XRD analysis confirms the formation of both pure FCC Ag and FCC Cu phases in all three compositions of bimetallic nanoparticles prepared.

To understand the nanostructures formed in bimetallic samples S2, S3 and S4, SEM EDX elemental mapping (Figure 6.2.2) of these nanoparticles has been carried out.

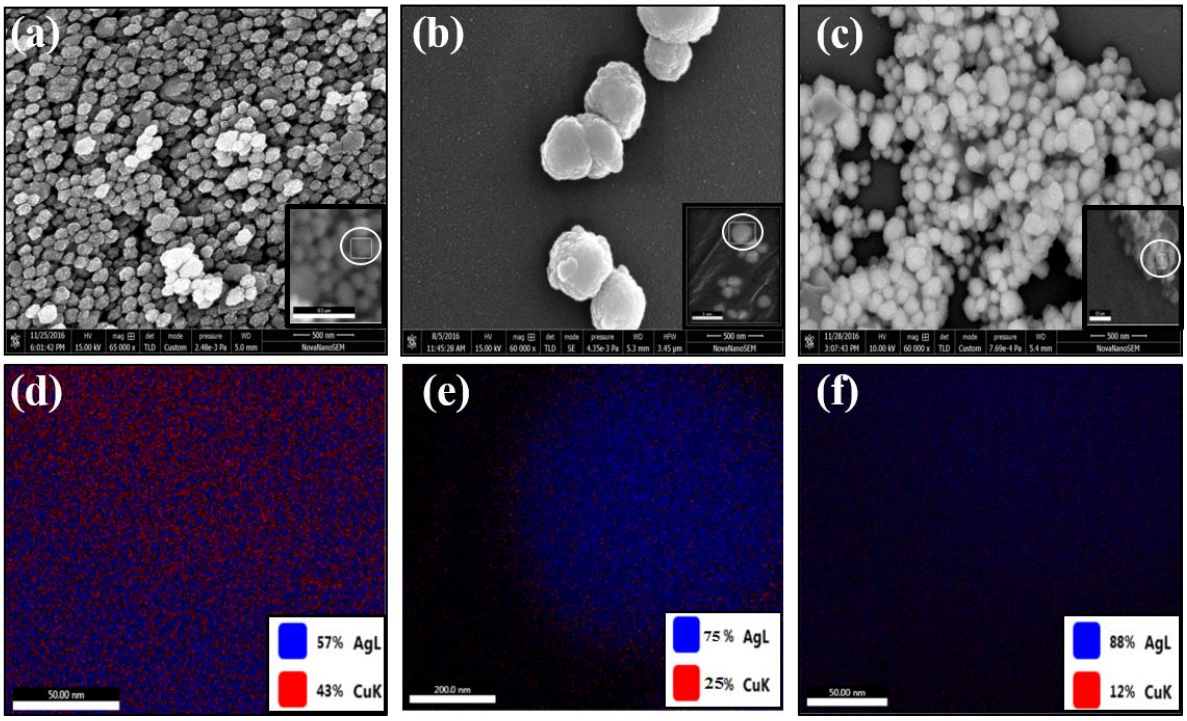


**Figure 6.2.2** HR-SEM images of S2, S3 and S4 Ag-Cu BNPs samples **(2 (a), 2 (b), 2 (c))** and corresponding elemental mapping of particles **(2 (d), 2 (e), 2 (f))** respectively. Particle on which mapping was done is shown in the inset of corresponding SEM image

Figures 6.2.2 (a), 2 (b) and 2 (c) show the SEM images for samples S2, S3 and S4 Ag-Cu BNPs respectively. The inset of each SEM image shows the particular nanoparticle for which elemental mapping was done. The corresponding SEM EDX elemental mapping of

the samples S2, S3 and S4 Ag-Cu BNPs (Figures 6.2.2 (d), 2 (e) and 2 (f) respectively) display the presence of both Ag (depicted by blue pixels) and Cu (represented by red pixels) in the mapped nanoparticle. The Cu percentage decreases in the nanoparticle mapped as one progresses from S2 to S4. This is similar to those observed in Ag-Cu BNPs by Jiang *et al.* (2005).

Figure 6.2.3 displays the TEM micrograph of S1, S2, S3, S4 and S5 samples. Nanoparticles in TEM images of S2 and S3 consist of anisotropic as well as spherical shapes. Furthermore, different types of anisotropic shapes are observed. On the other hand, sample S4 consists of roughly spherical nanoparticles only. The average size of Ag-Cu BNPs in samples S2, S3 and S4 is found to be ~ 110, ~ 380 and ~ 72 nm respectively. Particle size distributions for these samples are given in inset of corresponding TEM micrographs (Figure 6.2.3). The number of nanoparticles sampled for arriving at this distribution was approximately ~ 150.

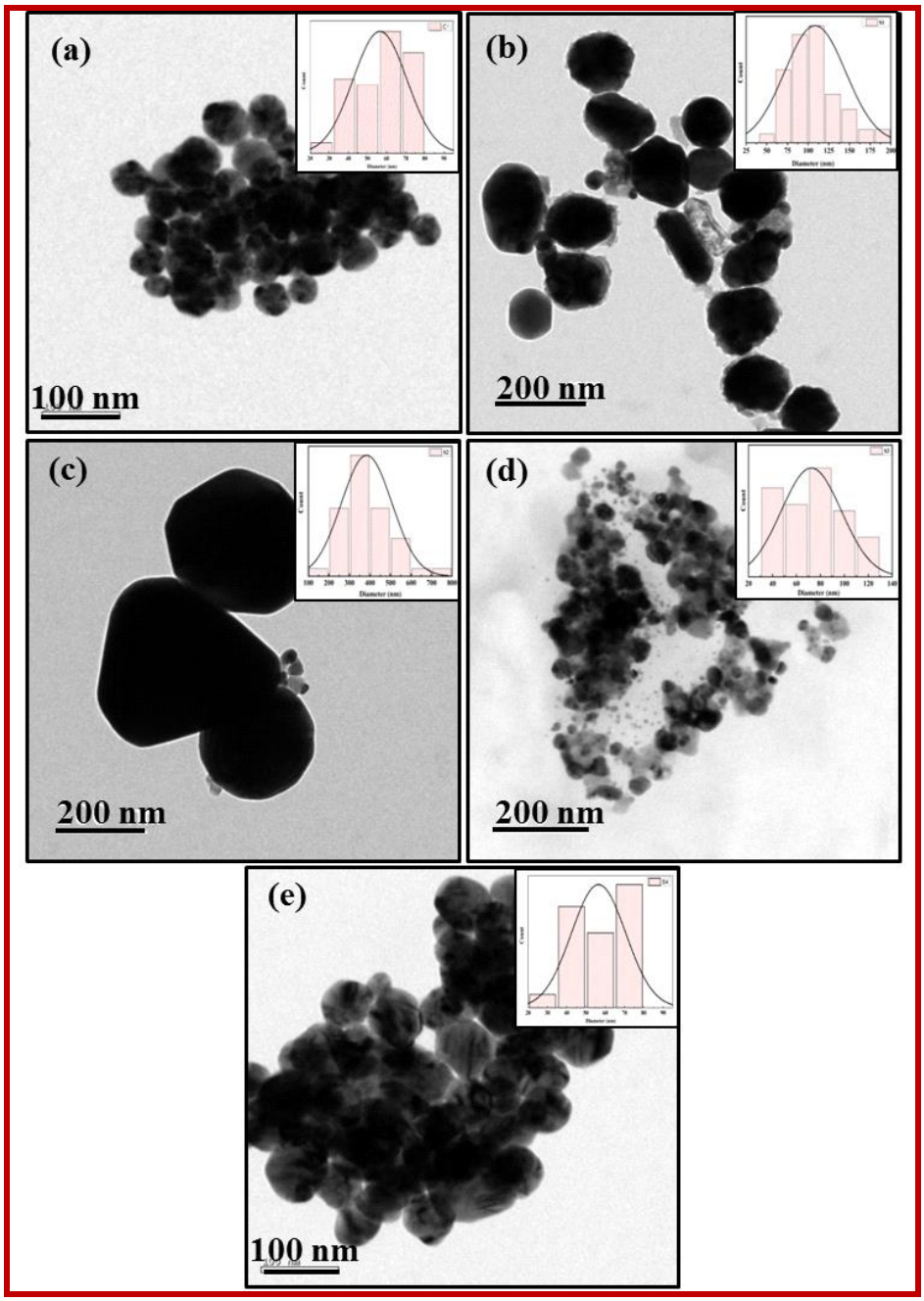


**Figure 6.2.3** TEM images of S1, S2, S3, S4 and S5 samples are represented as **3 (a), 3 (b), 3 (c), 3 (d)** and **3 (e)** respectively, their corresponding size distribution histograms are shown in the inset of each micrograph

UV visible spectra of S1, S2, S3, S4 and S5 nanoparticle sols are shown in Figure 6.2.4 (a). It is well-known that pure Ag and Cu nanoparticles display localized surface

plasmon resonance (LSPR) absorbance maxima typically at around ~ 580 nm and ~ 420 nm respectively. Samples S1 and S5, pure Cu and Ag nanoparticles sols, display the same values of LSPR absorbances as mentioned above. However, S2, S3 and S4 samples prepared in the present investigation shows LSPR absorbance maxima at ~ 520 nm, ~ 487 nm and ~ 445 nm respectively (Figure 6.2.4).

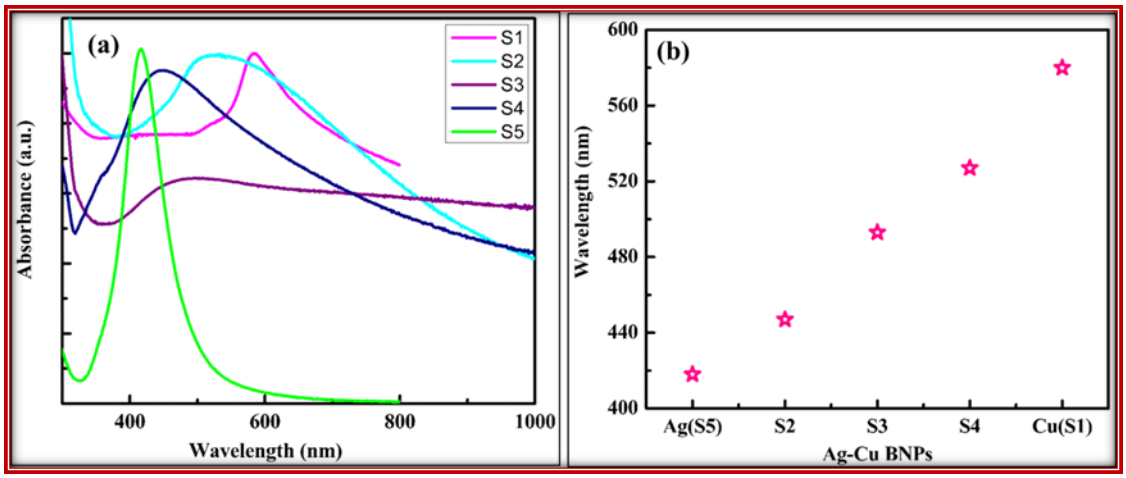


**Figure 6.2.4** The UV-Vis absorbance spectra of aqueous dispersion of S1 (CuNPs), S2, S3 & S4 (Ag-Cu BNPs) and S5 (AgNPs) sol samples **4(a)**, Maximum LSPR absorbances are plotted against precursor composition BNPs composition **4(b)**. An almost linear variation is obtained.

These absorbance maxima values lie between the absorption peaks of the pure Ag and pure Cu nanoparticles [Jiang *et al.* (2005)]. Furthermore, the LSPR maximum decreases with precursor Cu salt content. That is, it varies with the compositions of Ag and Cu present in the phase separated Ag-Cu BNPs. In view of the SEM EDX elemental mapping results of nanoparticles in samples S2, S3 and S4, such LSPR maxima value which lie between pure Ag and Cu LSPR values are due to both Ag and Cu elements coexists in the nanoparticles. That is, phase separated Ag-Cu BNPs with different phase compositions have been formed [Jiang *et al.* (2005)]. Another point to be noted is that the LSPR absorbance intensity of the

sol of sample S3 is less than that obtained for S2 or S4. This is because of the larger size of BNPs formed in S3. Furthermore, the LSPR absorbance of S3 decreases only slightly with increase in wavelength. This is due to the formation of anisotropic nanoparticles in S3. Transverse and longitudinal modes of LSPR of anisotropic BNPs give rise to such a broad LSPR absorbance spectrum.

The LSPR maxima obtained from the Figure 6.2.4 (a) are plotted against the precursor composition mole fractions in Figure 6.2.4 (b). This figure shows that the LSPR maxima vary almost linearly with the BNPs precursor composition. Such linear variation means that the Ag-rich and Cu-rich micro phase-separated domains (of ~ 2-3 nm size) are almost evenly distributed throughout the nanostructure that has been formed. Moreover, all nanoparticles prepared in these samples have such even distribution of these domains. Similar type of LSPR variation with Ag-Cu precursor composition was also demonstrated by Jiang *et al*. (2005).

### 6.2.4.2 Catalytic Activity of Ag-Cu BNPs for Nip reduction with $NaBH_4$ and Gly

The Nip reduction experiment is done with $NaBH_4$ as the reducing agent in presence of catalyst. Here the intensity of absorbance at ~ 402 nm (*p*-nitrophenolate ion) was found to decrease with time. Simultaneously, there was an increase in the intensity of a new absorbance peak at ~ 301 due However, in this case, the isosbestic points are not clear therefore further characterization was carried out to confirm the formation of AP.

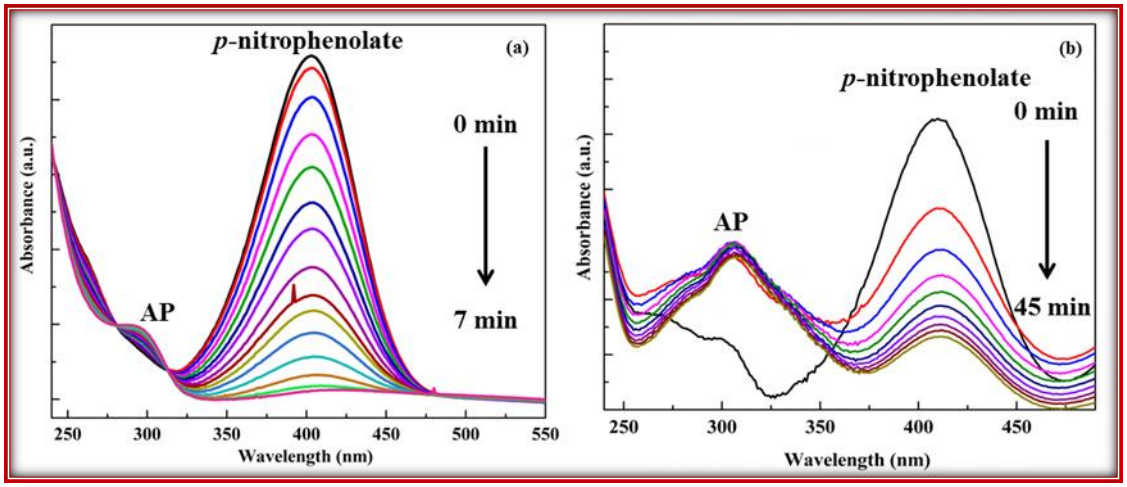


**Figure 6.2.5** UV-Vis absorption spectra for *p*-nitrophenol reduction by $NaBH_4$ **5(a)**, UV-vis absorbance of *p*-nitrophenol reduction by glycerol versus time in presence of Ag-Cu BNPs catalyst **5(b)**.

First azo- dye test was carried out as per the procedure given in reference [Vogel (1978)]. Formation of orange colored azo dye indicated the presence of aromatic amine functional group. Next, $^1$HNMR spectrum of the product (Figure 6.2.6) was measured in DMSO as solvent. The NMR peaks observed are δ 8.35 (s, 2 H), 7.27 – 5.02 (m, 4 H), 4.38 (s, 2 H) corresponding to three types of H present in AP.

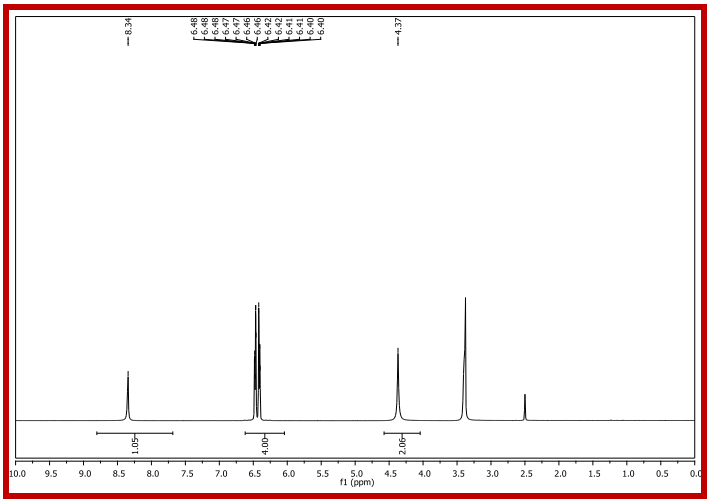


**Figure 6.2.6** NMR spectrum of AP, product of Nip reduction with glycerol in presence of S2 Ag-CuNPs.

**Reduction kinetics**

Using Eqn. 3 3 given in Chapter-3 the plot $\ln(\frac{\partial A}{\partial t})$versus $\ln(A)$ gives the order n with respect to reactant Nip [Alla *et al.* (2016), Gu *et al.* (2014)] for S1, S2, S3, S4 and S5 Cu, Ag-Cu BNPs and Ag catalysts. The value of n is found to be 2 when glycerol is the hydrogen source and the order is found to be 1 when $NaBH_4$is the reducing agent. Therefore, the kinetic plots between $\ln(A/A_0)$ and time are linear for S1, S2, S3, S4 and S5 catalyzed reactions when $NaBH_4$ is the reducing agent(Figure 6.2.7 (a)). Model Nip reduction by $NaBH_4$, in the presence of majority of the catalyst (monometallic or bimetallic) follows pseudo first order kinetics. Therefore, the result obtained for the present catalyst is in agreement with the previous reports in literature [Herves *et al.* (2012), Ghosh *et al.* (2007)]. However, the reaction is second order with respect to Nip when the reducing agent is glycerol. In accordance with this, linear plots are obtained between $1/A_t$ and time for S1, S2, S3, S4 and S5 catalyst (Figure 6.2.7 (b)).

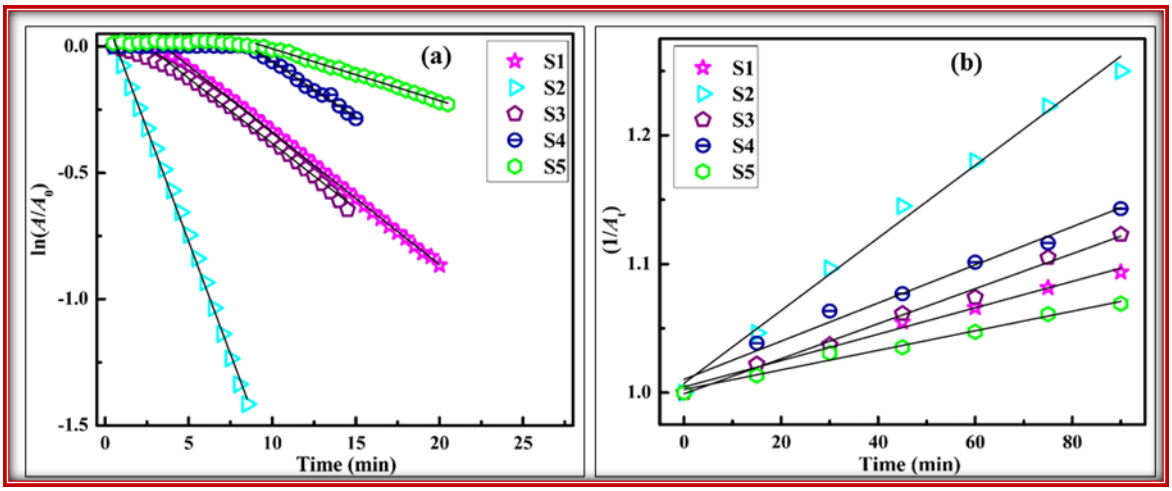


**Figure 6.2.7** Catalytic kinetics plots using S1, S2, S3, S4 and S5 Cu, Ag-Cu BNPs and Ag as catalysts, plot of $\ln(A/A_0)$ [absorbance ($A$) measured at $\lambda_{max}$ ~ 401 nm] versus time when $NaBH_4$ is the reducing agent **7 (a)** and plot of $1/A_t$ [absorbance ($A$) measured at $\lambda_{max}$ ~ 406 nm] against time when glycerol is the hydrogen source **7 (b)**. The $R^2$ value for fitting is found to be ~ 0.96.

It is worthwhile to mention here that glycerol reduction of Nip was found to be second order as discussed in previous chapters for anisotropic AgNPs, c-AgNPs and CuNPs catalyst (Chapter-3, 4 and 5). The rate constant values are, therefore, determined from the slopes of the linear plots of $\ln(A/A_0)$ and $(1/A_t)$ with time for Nip reduction in presence of $NaBH_4$ and glycerol as the respective reducing agents.

An important feature of the kinetics plot for Nip reduction by $NaBH_4$ in presence of S1, S2, S3, S4 and S5 catalysts is that initially the absorbance of *p*-nitrophenolate did not change for some interval of time. The time during which no reduction took place is known as induction time ($t_{ind}$). The $t_{ind}$ increases from a few seconds for S2 to larger intervals of time for S3 and S4 and further increase for S5. Basically, it increases with the Ag content of the nanoparticles. This is primarily due to adsorption of oxygen on to the surface of Ag component on the surface of bimetallic nanoparticles [Signori *et al.* (2010)]. However, no induction time was observed for glycerol reduction of Nip. This is because of lower relative solubility of oxygen [Kutsche *et al.* (1984)] in aqueous solution of glycerol as compared to pure water.

The activation energies of Nip reduction by two different reducing agents ($NaBH_4$ and glycerol) with respect to S1, S2, S3, S4 and S5 catalyst is determined by studying the kinetics of these catalytic reactions at four different temperatures. The reaction rate increases with temperature for all prepared catalysts. The classical Arrhenius equation is utilized to determine the activation energies of catalyst Eqn. 3.4 given in Chapter-3. The plots between $\ln(k_{app})$ and 1/T in presence of $NaBH_4$ and glycerol as reducing agents are shown in Figure 6.2.8 (a) and 8 (b) respectively. The activation energy ($E_a$) is calculated from the slope ($-E_a/R$) of the linear fit of these plots.

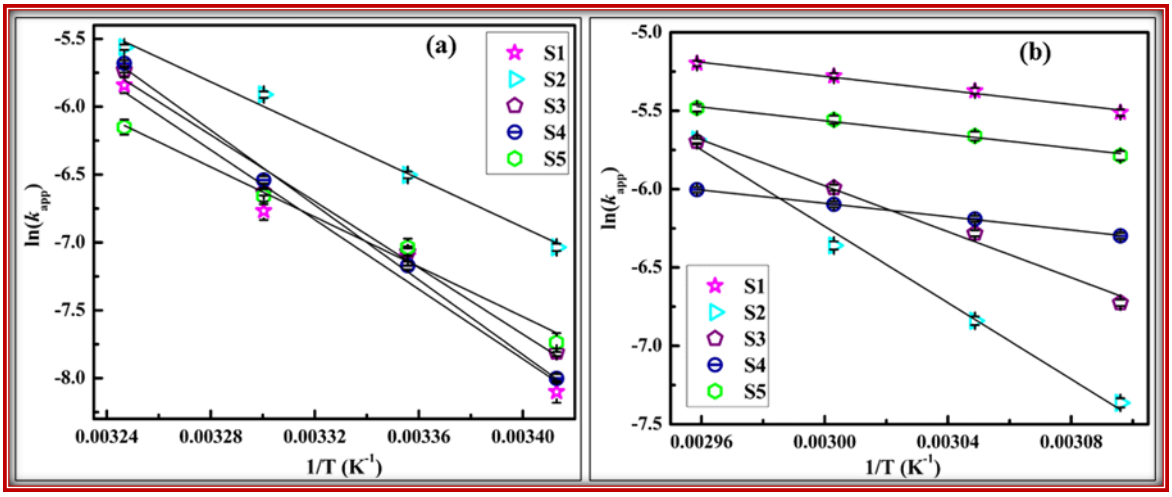


**Figure 6.2.8** Arrhenius plot for Nip reduction reaction catalyzed by S1, S2, S3, S4 and S5 catalyst, when $NaBH_4$ is used as hydrogen source **8 (a)** and when glycerol is used as hydrogen source **8 (b)**. Please note that for most data points, error bars are smaller than the size of the symbol used. The R2 value for fitting is found to be ~ 0.98.

The apparent reaction rate constant and activation energies found are tabulated in Table 6.2.1. TOF values for S1, S2, S3, S4 and S5 catalysts are calculated from Eqn.3.5 given in Chapter-3. The obtained values for all the catalysts are given in Table 6.2.1.

**Table 6.2.1 Catalytic activity parameters $k_{app}$, $E_a$ and TOF values for different catalysts.**

| Catalyst | Apparent reaction rate constant ($k_{app}$) | | Activation energy ($E_a$) (kJ/mol) | | Turn over frequency (TOF) ($min^{-1}$) | |
|---|---|---|---|---|---|---|
| | $NaBH_4$ ($min^{-1}$) | Gly ($mol^{-1}$ lit $min^{-1}$) | $NaBH_4$ | Gly | $NaBH_4$ | Gly |
| **S1** | 0.04 | 0.0031 | ~ 135.1 | ~ 18.8 | ~ 180 | ~ 3.6 |
| **S2** | 0.178 | 0.0028 | ~ 75.2 | ~ 100.1 | ~ 399 | ~ 5.0 |
| **S3** | 0.053 | 0.00136 | ~ 100.1 | ~ 62.9 | ~ 192 | ~ 3.5 |
| **S4** | 0.043 | 0.0014 | ~ 113.9 | ~ 17.8 | ~ 179 | ~ 2.7 |
| **S5** | 0.011 | 0.00209 | ~ 98.9 | ~ 18.4 | ~ 161 | ~ 1.3 |

When $NaBH_4$ is used as the reducing agent then the activation energy increases as we go from S2 to S3 and then S3 to S4 finally. That is, the activation energy increases with the Ag content in the Ag-Cu BNPs. Concurrently, the TOF values for these reactions decrease as we go from S2 to S4. Latter observation is in agreement with the increase in activation energy observation. Another important observation that needs to be mentioned here is that the TOF calculation includes the $t_{ind}$ and this is maxima for S3 and then decreases to a few seconds for S1. Figure 6.2.9 (a) shows the variation in TOF value with change in composition of the nanoparticles. One can see the peak in synergistic catalytic activity at 1 : 1 (Ag : Cu) ratio (sample S2). Furthermore, this effect decreases as the amount of Ag increases in the bimetallic NPs.

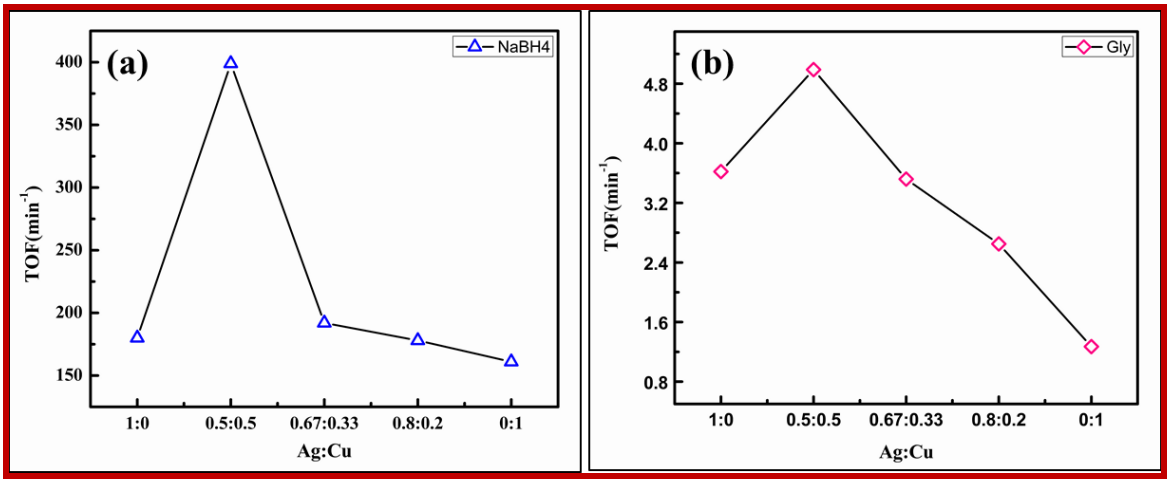


**Figure 6.2.9** Turnover frequency versus BNPs Ag : Cu composition when **9 (a)** $NaBH_4$ and **9 (b)** Glycerol is the reducing agent (points joined as a guide to eye only).

On the other hand, when glycerol is the reducing agent then the activation energies decrease from S2 to S4, that is, with increase in Ag component content in the Ag-Cu BNPs. The $E_a$ for S4 is found to be quite low. However, the TOF values also decrease with increase in Ag content from S2 to S4. Although S4 has smallest average nanoparticle size among the three Ag-Cu BNPs, still its TOF value is the lowest. This indicates that the number of active

sites available for catalyzing reduction by glycerol possibly decreases with increase in Ag component in the nanoparticles. Another, factor that may be affecting the TOF results may be the anisotropic shapes that are available in S2 and S3 but not in S4. The number of active sites contributed due to anisotropic shapes decreases with increase in size of the nanoparticles as we go from S2 to S3. Here also one observes synergistic enhancement in catalytic activity (from the TOF value) for S2.

The synergistic catalytic activity (for S2) could be because, at 1 : 1 precursor ratio, the micro phase-separated Ag-rich and Cu-rich domains are evenly surrounded by each other. In other words, there are more Ag-Cu phase boundaries in this nanostructure. It appears that these junctions or phase boundaries give rise to catalytic active sites. Hence, among the BNPs samples considered in this section, S2 has more phase boundaries and the maximum density of catalytically active sites. The $NaBH_4$ reduced Nip reaction catalyzed by S2 also has the lowest activation energy. The highest catalytic activity of S2 Ag-Cu BNPs is therefore due to both low activation energy and more number of active sites due to phase separated BNPs. But this is not so when Nip is reduced by Gly in presence of S2. In this case, therefore, the highest catalytic activity of S2 Ag-Cu BNPs is due to predominantly more number of active sites for this reaction in the S2 catalyst as well as zero induction time for Gly reduced Nip reaction.

#### 6.2.4.3 Photocatalytic Nip reduction with glycerol

Figure 6.2.9 compares the catalytic activity in presence and absence of visible light for each BNPs catalyst considered in this section. The catalytic activity values in terms of $k_{app}$, TOF and PTOF values are displayed in Table 6.2. In contrast to the photocatalytic

plasmonic enhancement of Gly reduction of Nip in presence of AgNPs and CuNPs (Chapter-3, 4 and 5), these Ag-Cu BNPs exhibit a completely opposite trend.

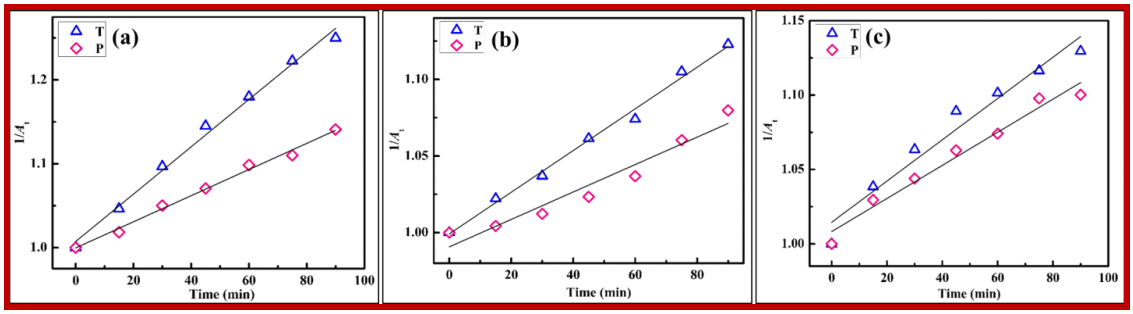


**Figure 6.2.10** Thermal (T) and photocatalytic (P) rate plots between $1/A_t$ versus time for Nip reduction with glycerol in presence of S2 **10 (a),** S3 **10 (b)** and S4 **10 (c)** Ag-Cu BNPs catalyst. The R2 value for fitting is found to be ~ 0.97.

**Table 6.2.2** Comparison of $k_{app}$ values for both thermal and photocatalytic Nip reduction by Gly in presence of S2, S3 and S4 Ag-Cu BNPs catalyst.

| **Catalyst** | **Apparent reaction rate constants ($k_{app}$) ($mol^{-1}$ lit $min^{-1}$)** | | **Turn over frequencies (TOF) ($min^{-1}$)** | |
|---|---|---|---|---|
| | **Thermal** | **Photocatalytic** | **TOF** | **PTOF** |
| **S2** | 0.0028 | 0.00156 | 4.99 | 4.12 |
| **S3** | 0.00136 | 0.00089 | 3.52 | 3.16 |
| **S4** | 0.00139 | 0.0011 | 2.65 | 2.45 |

Figures 6.2.10 (a), 10 (b) and 10 (c) show, first of all, that after exposure to visible light the catalytic activity of these systems for Nip reduction with Gly decreases. Second, the decrease in activity is most for S2. The decrease in activity is lesser for S3 and still lesser for S4. Therefore, as the Cu content in bimetallic decreases, the decrease in catalytic activity owing to exposure to visible light is also lesser. The surfaces of all three BNPs samples (S2, S3 and S4) are interspersed by Ag and Cu patches in a way that depends on their composition. It appears that the plasmonic excitation of electrons is quenched by the

neighboring Cu surface patch. The lesser the amount of Cu on the surface, lesser is the quenching.

### 6.2.4.4 Methyl orange oxidation thermal and photocatalytic

Figure 6.2.11 shows the UV-visible spectrum of MO degradation when the reaction is carried out in presence of S2 Ag-Cu BNPs catalyst. All three peaks present initially in the UV-visible spectrum of MO in acidic medium undergo degradation together with progress of time.

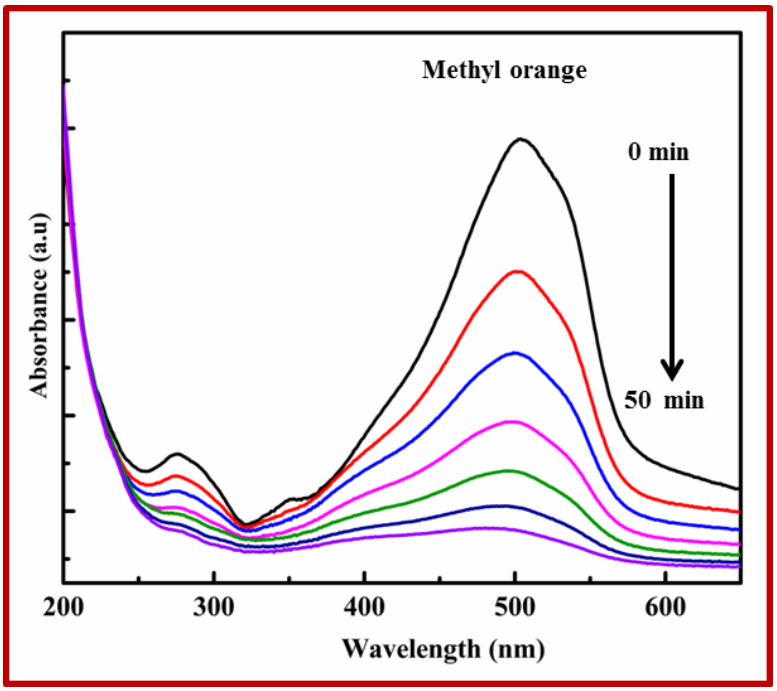


**Figure 6.2.11** Variation of absorbance maximum of MO (506 nm) with $H_2O_2$ oxidizing agent in presence of catalyst S2 Ag-Cu BNPs catalyst.

Besides, there is no new absorption peak is observed in this region, suggesting that MO degradation definitely occurs till the stage (E, F, G) of the well-known mechanism proposed in Chapter-3 (Figure 3.16).

For this oxidative MO degradation in presence of Ag-Cu BNPs, the order of reaction is obtained from the slope of the linear fit of plot between $\ln\left(-\frac{\partial A}{\partial t}\right)$ versus $\ln A$ following the procedure given in Chapter-3 [Eqn. 3.3]. The orders for both thermally and photocatalytically catalyzed MO degradations are equal to 2. Consequently, the respective $k_{app}$ values are found from the slopes of the linear fits for the plots between $1/A_t$ versus time for thermal and photocatalytic MO degradations (Figure 6.2.12).

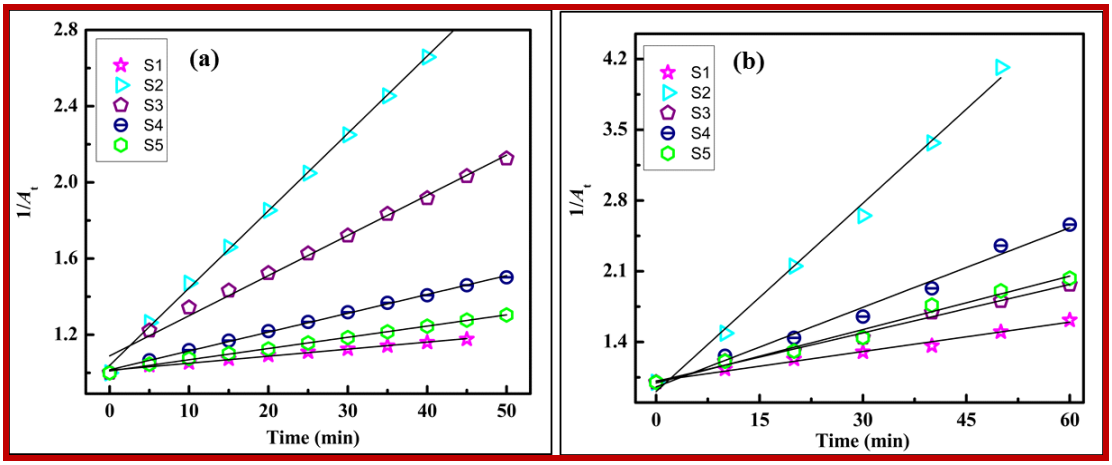


**Figure 6.2.12** Variation of $1/A_t$ [absorbance ($A$) measured at ~ 506 nm] versus time for thermal **12 (a)** and photocatalytic **12 (b)** MO degradation in presence of S1, S2, S3, S4 and S5catalyst. The $R^2$ value of all the fittings is ~ 0.97

Table 6.2.3 summarizes the thermal and photocatalytic $k_{app}$ associated with oxidative MO degradation in presence of S1, S2, S3, S4 and S5 catalyst. Further, this degradation was studied at different temperatures to calculate the activation energies by utilizing the linearized form of Arrhenius equation [Eqn.3.4 in Chapter-3]. The ln($k_{app}$) verses 1/T plots for all (S1, S2, S3, S4 and S5) catalyst samples obey good linear fits (Figure 6.2.13). The activation energy values for respective catalysts are calculated from the slopes (-$E_a$/R) of these linear fits. These values are also mentioned in Table 6.2.3.

**Table 6.2.3** Apparent reaction rate constant and turnover frequency (TOF) for thermal and photocatalytic MO degradation at 306 K in presence of S1, S2, S3, S4 and S5 catalyst are tabulated here. Activation energies for the thermally catalyzed reaction are also mentioned in column 4 of the Table.

| **Catalyst** | **Apparent reaction rate constant ($k_{app}$) ($mol^{-1}$ lit $min^{-1}$)** | | **Activation energy ($E_a$) (kJ/mol)** | **Turn over frequency (TOF) ($min^{-1}$)** | |
|---|---|---|---|---|---|
| | **Thermal** | **Photo** | | **TOF** | **PTOF** |
| **S1** | 0.003 | 0.005 | ~ 45.1 | ~ 1.0 | ~ 1.1 |
| **S2** | 0.040 | 0.050 | ~ 36.2 | ~ 5.0 | ~ 7.4 |
| **S3** | 0.020 | 0.017 | ~ 44.2 | ~ 2.9 | ~ 2.6 |
| **S4** | 0.009 | 0.020 | ~ 43.3 | ~ 1.8 | ~ 2.9 |
| **S5** | 0.0060 | 0.0097 | ~ 34.7 | ~ 1.3 | ~ 2.8 |

The $k_{app}$ value for S2 Ag-Cu BNPs is the highest for both thermal and photocatalytic MO oxidations. The catalytic and photocatalytic activities of these BNPs are quantified by their TOF and PTOF values in column-5 and 6 of Table. Here also, S2 shows synergistic catalytic activity (in terms of TOF and PTOF values) for oxidative MO degradation. As mentioned earlier, at 1 : 1 precursor ratio, the micro phase-separated Ag-rich and Cu-rich domains provide more Ag-Cu phase boundaries in S2 nanostructure. These phase boundaries are sources of catalytically active sites. Besides this, this catalyst also has lowest activation energy. The highest catalytic activity of S2 Ag-Cu BNPs is therefore due to both low activation energy and more number of active sites due to phase separated BNPs.

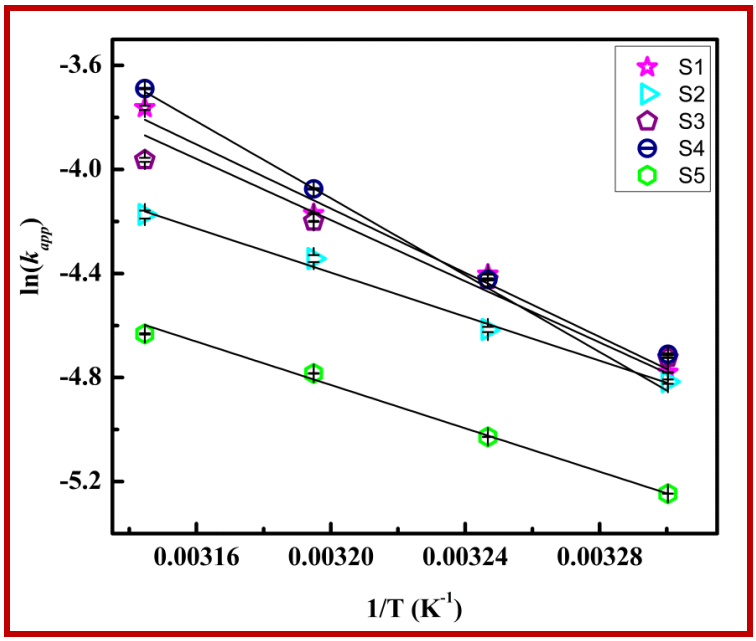


**Figure 6.2.13** Arrhenius plot for MO degradation catalyzed by S1, S2, S3, S4 and S5samples. Error bars are very small in most cases. The $R^2$ value of all the fittings is ~ 0.95.

Overall, the TOF values in Table 6.2.3 (column 5) follow the same trend as indicated by the $k_{app}$ values (column 2). As mentioned earlier, all these MO degradations were also carried out in presence of visible light. While no plasmonic photocatalytic enhancement in activity could be observed in case of Gly reduction of Nip, in case of MO degradation significant enhancement (50-70 %) could be observed for S2 and S4 BNPs samples. In case of S3, slight decrease in MO degradation catalytic activity in presence of light is observed. Figure 6.2.14 shows the variation in photocatalytic activity with BNPs composition. Synergistic photocatalytic activity is observed for sample S2. Similar effect is also observed when the reaction is done in absence of visible light.

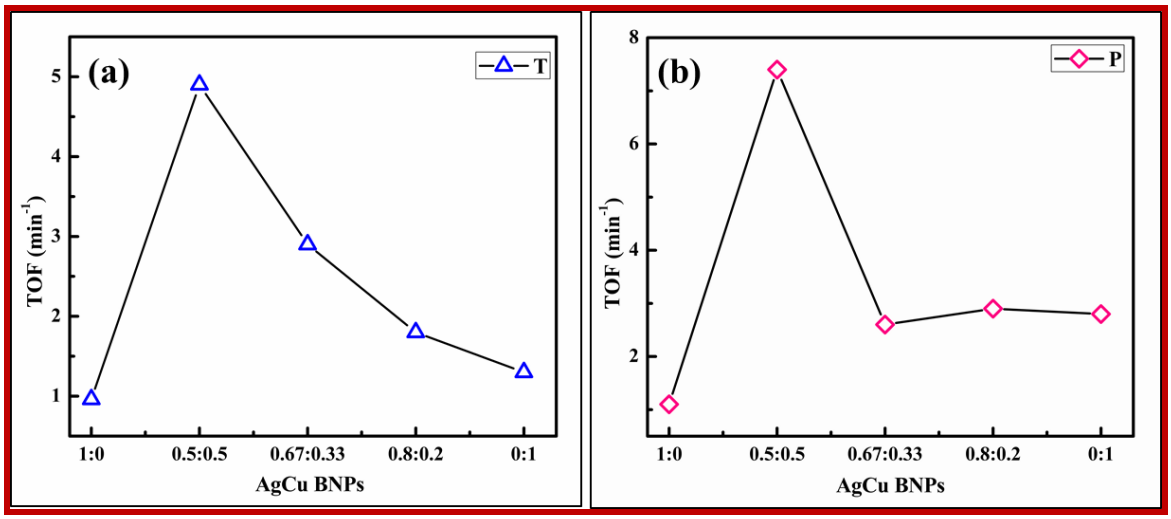


**Figure 6.2.14** Turnover frequency versus BNPs Ag : Cu composition when **14 (a)** Thermal and **14 (b)** Photocatalytic MO degradation was studied.

## 6.3 Catalytic studies of core shell Ag/Cu BNPs prepared by polyol method

### 6.3.1 Experimental details

#### 6.3.1.1 Synthesis of core shell Ag/Cu BNPs

To produce silver shell copper core (Cu@Ag) BNPs the following procedure was adopted. With continuous stirring 3.33 g of PVP (MW: 40000) was dissolved in 27.5 mL of EG solution in a 100 mL two-necked flask. The solution prepared was then heated to 383 K and maintained at this temperature for 1 h under $N_2$ bubbling condition to remove dissolved $O_2$ in the solution. The temperature of this solution was raised to 469 K. At this temperature 12 mL of 0.015 M $Cu(OAc)_2.7H_2O$ in EG was added dropwise to the PVP in EG solution using a syringe. The injection rate was 2 mL/min. The resulting solution was maintained at 196 $^0$C for 2.5 min until Cu seed nanoparticles are formed. This stage was indicated by change in color of the reaction mixture to reddish-brown. After this, 6 mL of 0.015 mM $AgNO_3$ solution in EG was injected at the rate of 6 mL/min. Heating of the reaction mixture

continued for 5 more minutes. Owing to heterogeneous nucleation, Ag precipitates on the surface of preexisting Cu seeds. The reaction mixture was then quenched in an ice bath. The sol thus prepared was initially characterized by UV-visible spectroscopy. The precipitate formed was separated out by centrifuging at 15000 rpm. Further, the precipitate was repeatedly washed with ethanol and then dried in vacuum oven at 50 $^0$C.

Copper shell silver core (Ag@Cu) BNPs were prepared by the following protocol. As per the foregoing procedure, first PVP in EG solution (at 469 K) was prepared. Next 12 mL of 0.015 M Ag($NO_3$) in EG was added to it in a dropwise manner to the PVP in EG solution using a syringe. The rate of injection was 2 mL/min. This solution was then heated at 196 $^0$C for 2.5 min to prepare Ag core NPs. Subsequently, 6 mL of 0.015 mM $Cu(OAc)_2.7H_2O$ solution in EG was injected at 6 mL/min rate to this reaction mixture. The reaction mixture was then quenched in ice bath. As mentioned above, the sol thus prepared was initially characterized by UV-visible spectroscopy. Then the precipitate formed was separated out by centrifuging, then subjected to repeated washing with ethanol and lastly vacuum dried at 323 K. These silver shell copper core (Cu@Ag)and copper shell silver core (Ag@Cu) BNPs are denoted as S6 and S7 BNPs respectively.

### 6.3.2 Catalytic reduction and oxidation

#### 6.3.2.1 Catalytic Nip reduction with $NaBH_4$

The experimental details for the Nip reduction with $NaBH_4$ in presence of core shell S6 and S7 BNPs catalyst is identical to the protocol described in sub-section 3.2.2.1 of Chapter-3.

#### 6.3.2.2 Catalytic Nip reduction with glycerol

The particulars of experiments for the Nip reduction with Gly as reductant in presence of core shell S6 and S7 BNPs as catalyst is identical to the protocol described in sub-section 3.2.2.2 of Chapter-3.

#### 6.3.2.3 Catalytic oxidation of MO dye

The experimental details for the oxidative MO degradation with $H_2O_2$ in presence of core shell S6 and S7 BNPs is identical to the protocol described in sub-section 3.2.2.3 of Chapter-3.

### 6.3.3 Visible light enhancement of catalytic reduction and oxidation activities

Photocatalytic activity was measured by placing the reaction mixtures in photocatalytic chamber as described in Chapter-2. The temperature of the photocatalytic chamber was measured to be 306 K.

#### 6.3.3.1 Photocatalytic enhancement of Nip reduction with glycerol

The reaction mixture with core shell S6 and S7 BNPs as catalyst was prepared as the procedure given in section 3.2.2.2. This reaction mixture is then irradiated by visible light from cool white LED source (approximately 940 watts/$m^2$) in the photocatalytic chamber at 306 K. The absorption spectrum of the reaction mixture was recorded after every 10 minutes time interval.

#### 6.3.3.2 Photocatalytic oxidation of methyl orange dye

The reaction mixture with core shell S6 and S7 BNPs as catalyst was prepared as by adopting procedure given in section 3.2.2.3. This mixture was kept in the photocatalytic

chamber at 306 K and then irradiated by visible light from cool white LED source (approximately 940 watts/$m^2$) to measure the kinetics and photocatalytic activities.

### 6.3.4 Results and discussion

#### 6.3.4.1 Characterization of core shell Ag/Cu BNPs

The UV–visible spectra of S6 and S7 BNPs sol samples are shown in Figure 6.3.1. Sample S6 BNPs show two absorbance maximum at ~ 438 and ~ 590 nm while sample S7 BNPs displays absorbance at ~ 444 and ~593 nm.

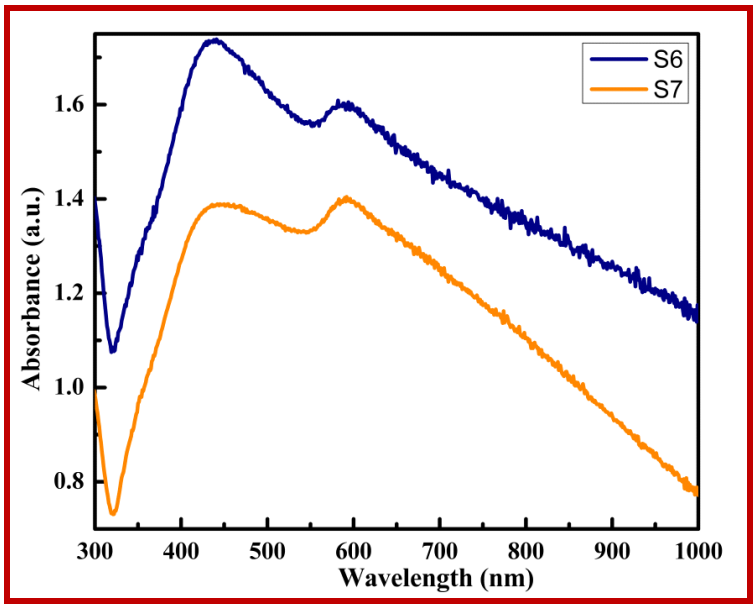


**Figure 6.3.1** The UV-Vis absorbance spectra of aqueous dispersion of core shell S6 and S7 BNPs sol samples.

In sample S6, the intensity of absorbance of Ag peak at ~ 438 nm is higher than that of Cu peak. This indicates that copper is in the core and the shell is made up of Ag. On the other hand, the UV-visible of S7 shows an LSPR peak for Cu (at ~ 593 nm) which has

intensity slightly higher than that observed for Ag (at ~ 444 nm). Since, it is well known that the LSPR of AgNPs is of higher intensity than that of CuNPs (of similar sizes), therefore, it may be summarized that in BNPs in S7 have a Ag core and Cu shell [Tsuji *et al.* (2010)]. Another important point to be noted is that with increase in shell thickness, the intensity of LSPR absorbance of the core component decreases [Navas and Soni (2015)]. However, in S6 the LSPR of the Cu component is appreciable. Similar is the case with S7, where the LSPR maximum intensity of Ag component, which makes up the core, is also appreciable. These observations lead us to believe that the shell thicknesses in both S6 and S7 may not be thick.

X-ray diffraction patterns of the nanoparticle powder samples S6 and S7 BNPs are shown in Figure 6.3.2. Both core shell, S6 and S7 BNPs samples shows five peaks at 38.12°, 44.43°, 64.68°, 77.07° and 81.24° which correspond to the {111}, {200}, {220}, {311} and {222} planes of FCC silver.

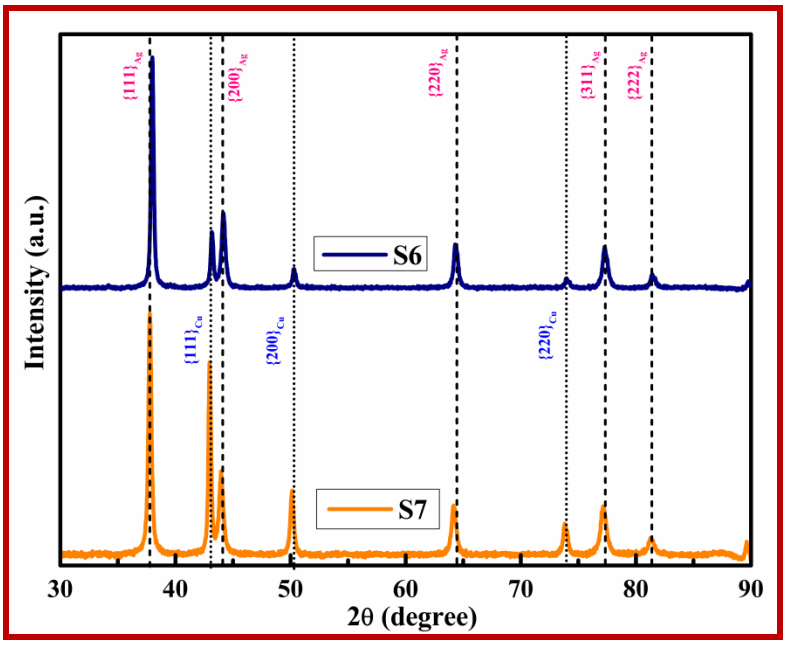


**Figure 6.3.2** X-ray powder diffraction patterns of core shell S6 and S7 BNPs samples.

Moreover, three peaks at 43.23°, 51.02° and 74.13° corresponding to {111}, {200} and {220} planes of FCC copper are also observed. Thus, XRD analysis confirms the formation of both pure FCC Ag and FCC Cu phases in both S6 and S7.These XRD patterns (for S6 and S7) are normalized with respect to the maximum intensity obtained in each case. This enables comparison between the intensities of the peaks of corresponding phases in the two XRD patterns and additional conclusions on the type of core shell nanostructure formed could be inferred. Thus, a comparison of the intensities of Cu {111} planes in S6 and S7 shows that it is much lesser in S6. The signal in the XRD patterns for the core of core shell particles get attenuated due to absorption of X-rays by the shell coating [Camardese *et al.* (2014), Westsson and Koper (2014)]. Therefore, lower intensities of Cu {111} plane peak in the XRD of S6 confirm that Cu forms the core of S6. Similarly, the higher relative intensities of Cu planes in S7 mean that Cu forms the shell of the BNPs in S7.

Further, HR-SEM and TEM images of S6 and S7 BNPs are given in Figure 6.3.3. Large faceted BNPs, of average size ~ 220 nm, are formed in S6. The nanostructures formed in S7 are of similar sizes. However, many of these nanostructures have a doughnut type shape. Please note, because of their outer and inner surfaces, such shapes have more surface area than spherical nanoparticle of similar size. Therefore, S7 BNPs would have access to more surface areas and there by higher number of surface active sites.

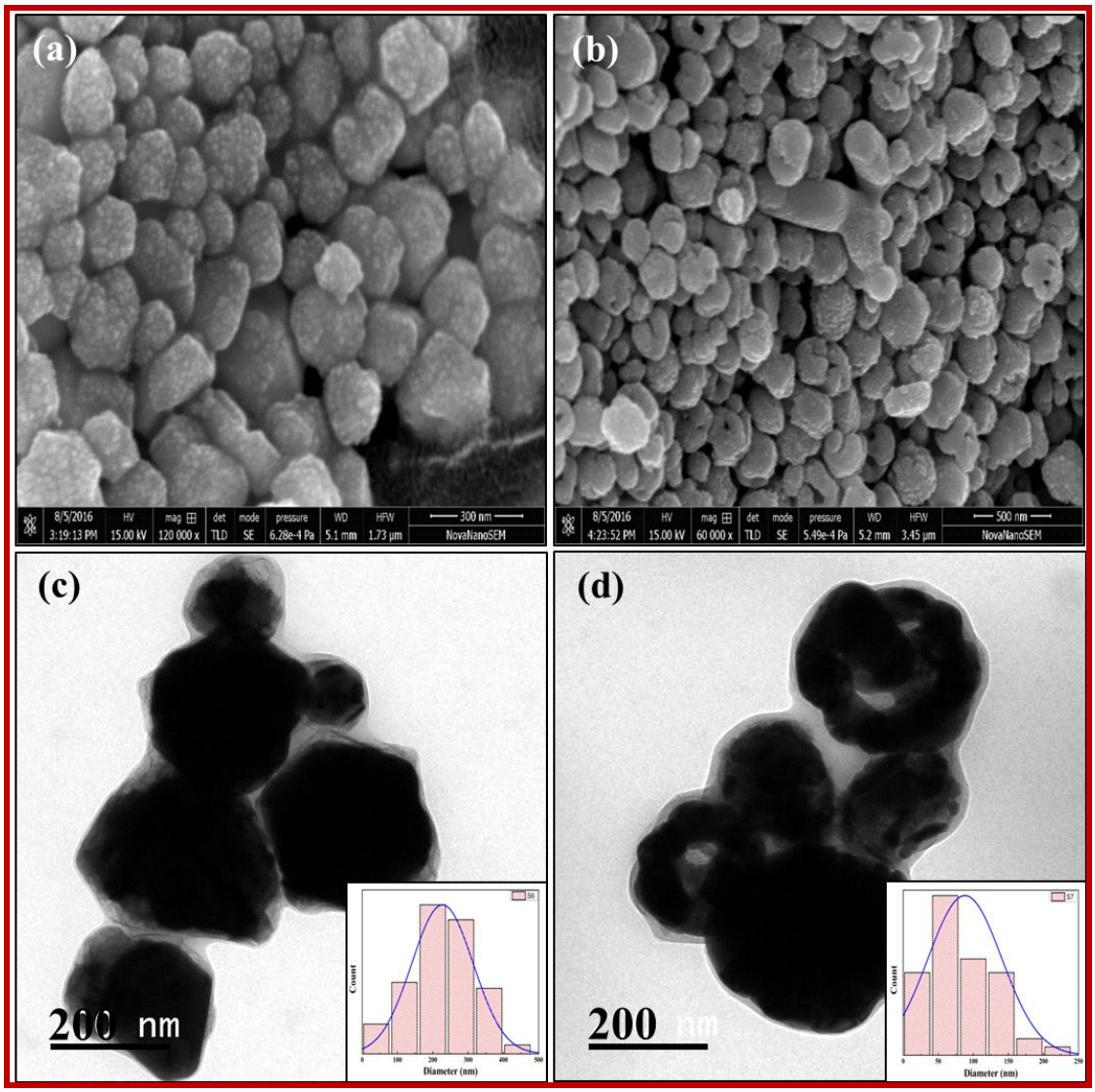


**Figure 6.3.3** HR-SEM images of S6 **3(a)** and S7 **3(b)** BNPs samples. TEM micrographs of S6 **3(c)** and S7 **3(d)** core shell BNPs sample, their corresponding particle size distribution histograms are shown in inset of respective TEM micrographs.

### 6.3.4.2 Catalytic Nip reduction with $NaBH_4$ and Gly

Figure 6.3.4 (a) shows that the intensity of absorption peak at ~ 400 nm decreased with time because of Nip reduction by $NaBH_4$ in presence of S6 BNPs catalyst. Simultaneously, a smaller absorbance maximum at ~ 301 nm gradually increased with time.

This was due to the formation of the reaction product AP. Also, the spectrum shows two isosbestic points at ~ 283 and ~ 312 nm which indicate that Nip fully converts to AP without any side reaction [Kaur *et al*. (2016)]. The time evolution of the UV-visible spectrum for Nip reduction by Gly in presence of S6 catalyst is shown in Figure 6.3.4 (b).

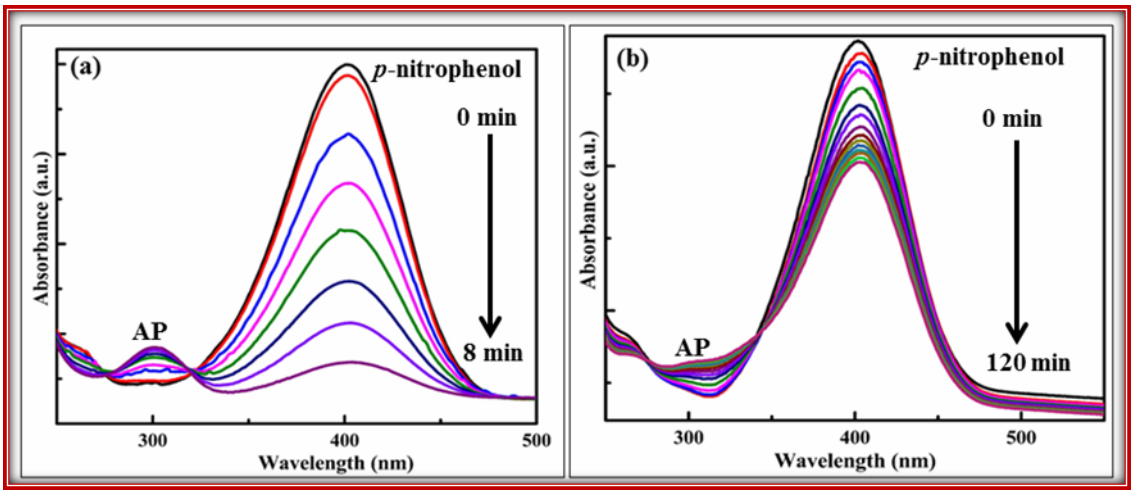


**Figure 6.3.4** UV-Vis absorption spectra for *p*-nitrophenol reduction by $NaBH_4$ **4 (a)**, UV-vis absorbance of *p*-nitrophenol reduction by glycerol versus time in presence of core shell BNPs catalyst **4 (b)**.

The absorbance maximum of *p*-nitrophenolate at ~ 406 nm is seen to decrease with time. Concurrently, the absorbance at ~ 306 nm increases due to formation of AP. Since the isosbestic points are not very clear, therefore, the product was further confirmed by a preliminary qualitative analysis and then $^1$HNMR was carried out to identify the actual product formed. The preliminary identification of presence of aromatic amine functional group was done by the azo dye test [Vogel (1978)]. This test resulted in the formation of orange colored azo dye which indicates the formation of *p*-aminophenol. Afterwards, $^1$HNMR of the product was carried out in DMSO solvent (Figure 6.3.5). The $^1$HNMR spectrum gives peaks at δ 8.35 (s, 2 H), 7.27 – 5.02 (m, 4 H), 4.38 (s, 2 H). These are in

agreement with three types of hydrogens (H) present in AP. This confirms the formation of AP in the product.

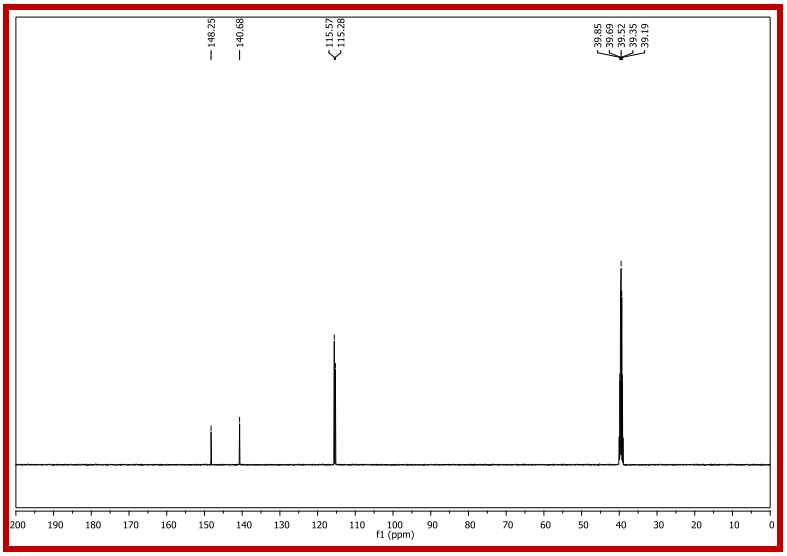


**Figure 6.3.5** NMR spectrum of product of Nip reduction with glycerol in presence ofS6 BNPs catalyst

**Reduction kinetics**

The slope of the linear fit of plot between $\ln(-\frac{\partial A}{\partial t})$ versus $\ln(A)$ [from Eqn.3.3] gives the order n with respect to reactant Nip [Alla *et al.* (2016), Gu *et al.* (2014)]. Since, the reducing agent ($NaBH_4$) taken for reduction is in excess (~ 40 times) as compared to Nip concentration, therefore the concentration of the reductant remains almost constant during the reaction. The order with respect to Nip, determined in this way for its reduction by $NaBH_4$, was found to be 1 for both S6 and S7 BNPs. Hence, this catalytic Nip reduction follows pseudo first order kinetics. In keeping with this, a $\ln(A/A_0)$ versus time plot was plotted (Figure 6.3.6 (a)). This plot shows that initially there was a time gap (the induction time

($t_{ind}$)) during which no reduction took place. Thereafter, a nice linear fit to the plot, in accordance with pseudo first-order kinetics, was obtained Figure 6.3.6 (a). The apparent rate constant ($k_{app}$) was determined from the slope of the linear fit of ln($A/A_0$) with time (after excluding $t_{ind}$). The $k_{app}$ value is larger for S7.

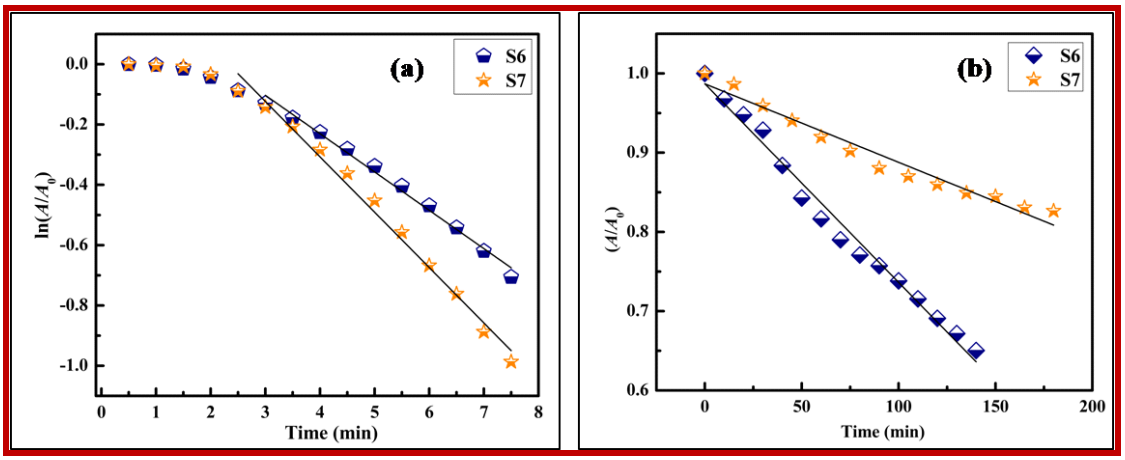


**Figure 6.3.6** Variation of ln($A/A_0$) [absorbance ($A$) measured at ~ 401 nm] Vs time with $NaBH_4$ reductant **6 (a)**. Variation of A/A0 [absorbance ($A$) measured at ~ 406 nm] Vs time with Gly as reductant in presence of both core shell S6 and S7 catalyst **6 (b)**. The $R^2$ value of all the fittings is ~ 0.98

The activation energies for this reduction in presence of core shell catalyst were found by measuring the kinetics of these reactions at different temperatures. As per the linearized Arrhenius equation [Eqn.3.4], the ln($k_{app}$) values are plotted against 1/$T$ in Figure 6.3.7. A good linear fit could be obtained to the plotted data points. The slope (-$E_a$/R) of the linear fit to this plot gives the activation energy values for this Nip reduction in the presence of different catalysts. These values are mentioned in column 5 and 6 of Table 6.3.1. The activation energy value for S7 is about 10 % lower than the value obtained for S6. More than

this, the higher surface area and thereby more catalytically active sites in S7 due to doughnut shaped nanostructures, appear to be responsible for the higher $k_{app}$ and TOF values for S7.

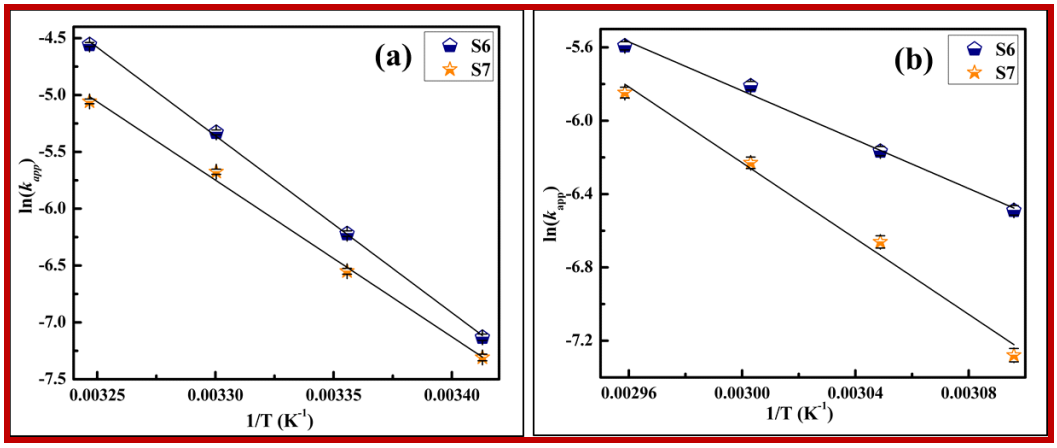


**Figure 6.3.7** Arrhenius plot for Nip reduction reaction catalyzed by S6 and S7 core shell catalyst samples with reducing agents $NaBH_4$ **7 (a)** and Gly **7 (b)**. Error bars are very small in most of the cases. The $R^2$ value of all the fittings is ~ 0.98.

On the other hand, when Gly was the reductant taken in excess, the value of order found with respect to Nip was 0 for both S6 and S7 BNPs. The order of reaction is found to be different from the (Nip) orders found for AgNPs catalysed Nip reduction with Gly mentioned in the previous chapters. However, the order is same as that obtained for CuNPs catalysed Nip reduction by Gly. Accordingly, the $k_{app}$ values are determined from the slopes of the linear fit of ($A/A_0$) against time shown in Figure 6.3.6 (b) and the values obtained are mentioned in Table 6.3.1. This value is higher for Nip reduction by Gly with S6 catalyst. This is contrary to the result obtained when the reduction was carried out with $NaBH_4$. The activation energy for Nip reduction by Gly is lower in case of S6. It appears that this is responsible for the higher catalytic activity of S6.

**Table 6.3.1** Average particle size, apparent reaction rate constants and activation energy for Nip reduction with $NaBH_4$ and Gly as reducing agent in presence of both S6 and S7BNPs catalyst.

| Catalyst | Particle size | Apparent reaction rate constant ($k_{app}$) | | Activation energy ($E_a$) (kJ/mol) | |
|---|---|---|---|---|---|
| | d (nm) | $NaBH_4$ ($min^{-1}$) | Gly ($mol\,lit^{-1}min^{-1}$) | $NaBH_4$ | Gly |
| **S6** | ~ 210 | 0.127 | 0.0025 | ~ 129.3 | ~ 51.1 |
| **S7** | ~ 90 | 0.183 | 0.00099 | ~ 115.2 | ~ 86.2 |

### 6.3.4.3 Photocatalytic study

The order of reaction in photocatalytic Nip reduction with Gly (as the reductant in excess) follows second order kinetics (Figure 6.3.8). This is different from zero order, with respect to Nip, followed in the thermally catalyzed reduction. It is an indication that the mechanisms followed for visible light photocatalytic Nip reduction and for this reduction by Gly in absence of light are dissimilar. Since, photocatalytic Nip reduction follows second order kinetics, therefore, the $k_{app}$ values are obtained from the slope of the linear fit of $1/A_t$ versus time plot. The $k_{app}$ and PTOF values of photocatalytic Nip reduction with glycerol are tabulated in column 2 of Table 6.3.2. The $k_{app}$ and PTOF values show that S6 BNPs has higher photocatalytic activity compared to S7. For the sake of comparison, the TOF values of core shell BNPs catalysts for Nip reduction with Gly (in absence of light) have been repeated in Table 6.3.2. Although, the order (w. r. t Nip) is different for the photocatalytic and

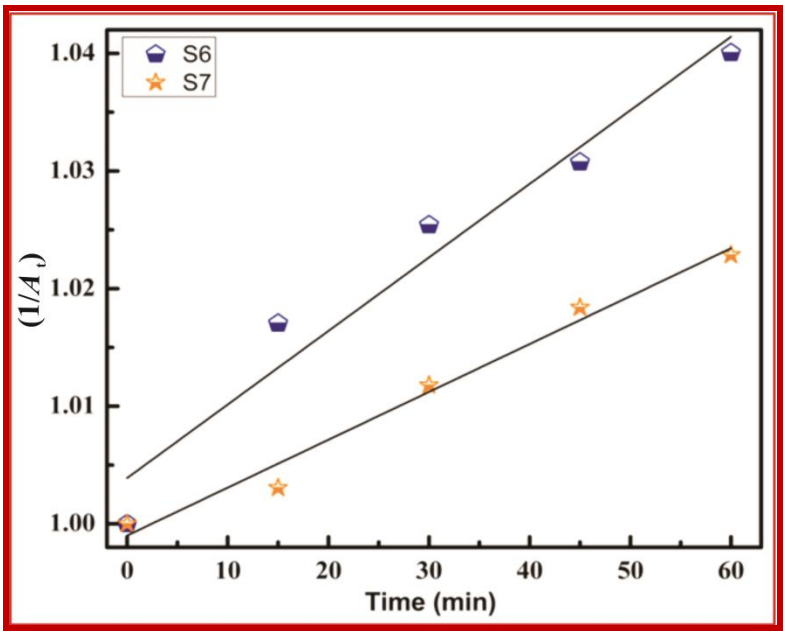


**Figure 6.3.8** Variation of $1/A_t$ [absorbance ($A$) measured at ~ 406 nm] Vs time with Gly as reductant in presence of both S6 and S7 catalyst. The $R^2$ value of all the fittings is ~ 0.96.

**Table 6.3.2** Displays the photocatalytic apparent reaction rate constant, photocatalytic turnover frequency (PTOF) and TOF for Nip reduction with Gly as reducing agent at 306 K.

| **Catalyst** | **Photocatalytic apparent reaction rate constant ($k_{app}$) ($mol^{-1}$ lit $min^{-1}$)** | **Turn over frequency ($min^{-1}$)** | |
|---|---|---|---|
| | | **TOF** | **PTOF** |
| **S6** | 0.003 | ~ 26.0 | ~ 32.0 |
| **S7** | 0.0013 | ~ 9.0 | ~ 14.0 |

thermally catalyzed cases, the PTOF and TOF values follow the same trend. That is, S6 exhibits higher photocatalytic activity than S7. There is 20-40 % photocatalytic enhancement when the reaction is carried out under visible light. Furthermore, it is important to emphasize that overall both thermally as well as photocatalytic Nip reduction by Gly reductions show drastic increase in catalytic activity when such core-shell nanostructures are used (in comparison to pure Ag or Cu NPs). Visible light photocatalytic enhancements for both S6

and S7 mean that in both cases plasmonic excitation of electrons does take place. It appears that the Ag shell of S6 BNPs has higher density of catalytically active centers for Gly reduced Nip reaction. That is reason for higher catalytic activity of S6 for Gly reduced Nip. Since the shell is thin, therefore, the Cu core harvested visible light photons are able to channel that energy into the catalytically active centers on the nanostructure shell [Aslam *et al.* (2017)].

### 6.3.4.4 Methyl orange oxidation thermal and photocatalytic

The UV-visible spectrum for MO degradation with time in presence of S6 BNPs is shown in Figure 6.3.9. All three peaks present initially in the UV-visible spectrum of MO in acidic medium undergo degradation together with progress of time.

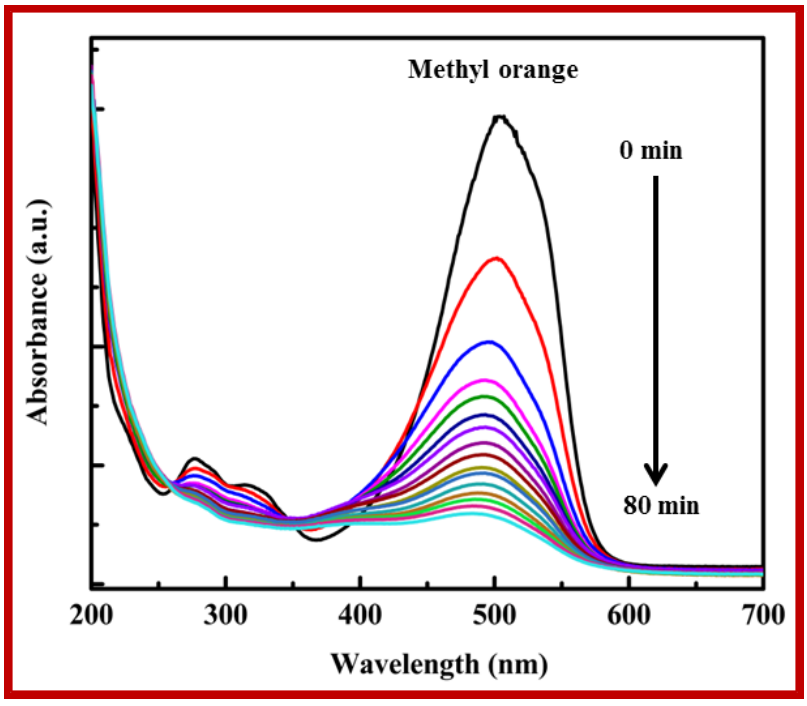


**Figure 6.3.9** Variation of absorbance maximum of MO (~ 506 nm) with $H_2O_2$ oxidizing agent in presence of catalyst S6 BNPs catalyst

No new absorption peak could be observed in the UV-visible spectrum during the oxidative degradation. The order n of MO degradation obtained following the procedure outlined

earlier [Eqn. 3.3]. is found to be 2 and 0 for thermally and photocatalytically catalyzed MO degradations (using both S6 and S7 respectively). Consequently, the respective $k_{app}$ values are found from the slopes of the linear fits for the plots between $1/A_t$ versus time for thermal and $A/A_0$ versus time photocatalytic MO degradations (Figure 6.3.10).

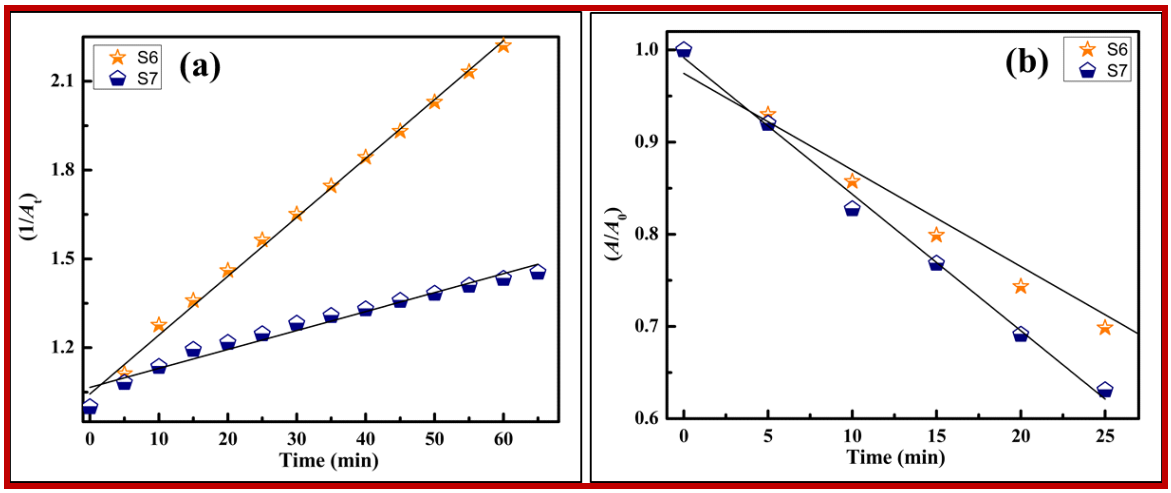


**Figure 6.3.10** Variation of $1/A_t$ [absorbance ($A$) measured at ~ 506 nm] versus time for thermal **10 (a)** and Variation of $A/A_0$ [absorbance ($A$) measured at ~ 506 nm] versus time for photocatalytic **10 (b)** MO degradation in presence of S6 and S7 BNPs catalyst. The $R^2$ value of all the fittings is found to be ~ 0.97.

The thermal and photocatalytic apparent reaction rate constants associated with oxidative MO degradation in presence of core shell catalyst are summarized in Table 6.3.3. Further, this degradation was studied at different temperatures to calculate the activation energies by utilizing to linearized the Arrhenius equation given in Chapter-3 [Eqn. 3.4] (Figure 6.3.11) versus time). Though the order of reactions is different in thermally and photocatalytically catalyzed MO oxidation reaction, the catalytic activity trend remains the same whether the reaction is carried out in presence or absence of light.

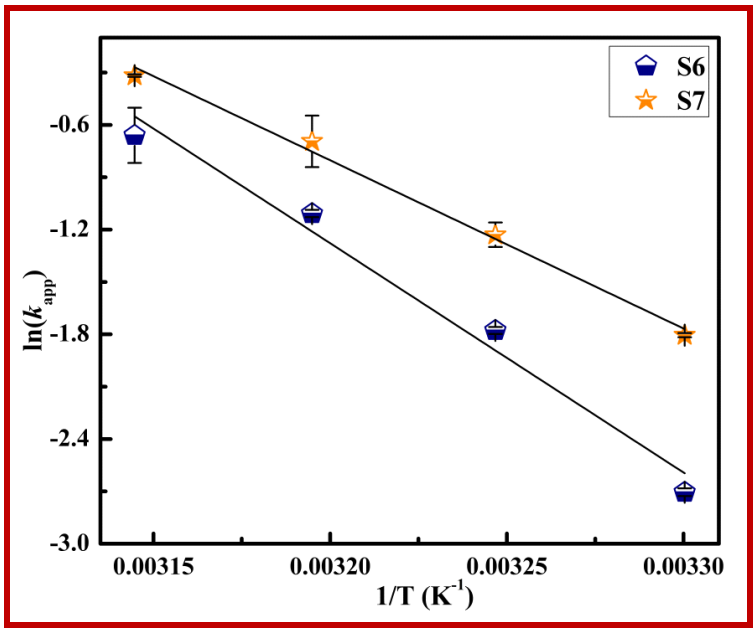


**Figure 6.3.11** Arrhenius plot for MO degradation catalyzed by S6 and S7 BNPs samples. Error bars are very small in most cases. The $R^2$ value of all the fittings is ~ 0.98

**Table 6.3.3.** Apparent reaction rate constant, activation energy and turnover frequency (TOF) for thermal and photocatalytic MO degradation at 306 K in presence of both S6 and S7 BNPs catalyst.

| Catalyst | Apparent reaction rate ($k_{app}$) | | Activation energy ($E_a$) (kJ/mol) | Turn over frequency ($min^{-1}$) | |
|---|---|---|---|---|---|
| | Thermal ($mol^{-1}$ lit $min^{-1}$) | Photo (mol $lit^{-1}min^{-1}$) | | TOF | PTOF |
| **S6** | 0.011 | 0.019 | ~ 109.1 | ~ 4.0 | ~ 7.4 |
| **S7** | 0.0064 | 0.0148 | ~ 81.2 | ~ 2.1 | ~ 5.0 |

In both thermally catalyzed and photocatalytic conditions, the $k_{app}$ and TOF (or PTOF) values for S6 are higher than that of S7 BNPs catalyst. Moreover, on comparing the TOF and PTOF values, it can be seen that there is large visible light photocatalytic enhancements for both S6 and S7.This means that for both S6 and S7 plasmonic excitation of

electrons do occur which possible result in oxidative degradation of MO by the mechanism proposed in Chapter-3.

## 6.4 Catalytic study of Ag-Cu BNPs prepared by reduction of $Ag(NH_3)_2^+$ with $Cu^{2+}$ salt

### 6.4.1 Experimental details

#### 6.4.1.1 Synthesis of Ag-Cu BNPs

Materials used for the synthesis of Ag-Cu BNPs were $Ag(NO_3)$ (Merck), $Cu(NO_3)_2.3H_2O$ (Merck), Polyvinylpyrrolidone (PVP) (Himedia), NaOH (Merck), Ammonia (Merck) and Hydrazine Hydrate (Merck). All reagents used were of analytical reagent grade and used without further purification. Equal volumes of 0.0125 M NaOH and 0.25 M hydrazine hydrate were mixed to prepare the alkaline hydrazine hydrate (AHH) solution. Equal volumes (10 mL each) of 5 wt % PVP aqueous solution and 0.05 M $Cu(NO_3)_2.3H_2O$ aqueous solution were mixed in a conical flask. This reaction mixture flask was kept in a preheated water bath maintained at 333 K. Then 16 mL of AHH solution was added in a dropwise manner to this reaction mixture with continuous stirring. On AHH addition the initially blue colored copper salt solution changes to orange. At this stage 5 mL of $Ag(NH_3)_2$ complex (prepared by adding equal volumes of 0.05 M $Ag(NO_3)$ solution and 0.1 M $NH_3$ solution) solution was added and the stirring was continued for further 30 min at 333 K. Finally, a reddish-brown color precipitate was obtained. The precipitate was separated by centrifuging at 15000 rpm. It was further washed repeatedly with ethanol and then vacuum dried at 323 K. Two Ag-Cu BNPs samples were prepared in this manner. These have been denoted samples S8 and S9. In S8 the copper salt solution to $Ag(NH_3)_2^+$ solution ratio is 2 : 1.The initial copper salt solution to $Ag(NH3)_2^+$ solution in sample S9 is 4 : 1.

### 6.4.2 Catalytic reduction and oxidation

#### 6.4.2.1 Catalytic Nip reduction with $NaBH_4$

The experimental detail for Nip reduction by $NaBH_4$ in presence of S8 and S9 Ag-Cu BNPs is identical to the protocol described in sub-section 3.2.2.1 of Chapter-3.

#### 6.4.2.2 Catalytic Nip reduction with glycerol

The particulars of experiments for the Nip reduction with Gly as reductant in presence of phase separated S8 and S9 Ag-Cu BNPs as catalyst is identical to the protocol described in sub-section 3.2.2.2 of Chapter-3.

#### 6.4.2.3 Catalytic oxidation of MO dye

The experimental details for the oxidative MO degradation with $H_2O_2$ in presence of S8 and S9 Ag-Cu BNPs are identical to the protocol described in sub-section 3.2.2.3 of Chapter-3.

### 6.4.3 Visible light enhancement of catalytic reduction and oxidation activities

Photocatalytic activity was measured by placing the reaction mixtures in photocatalytic chamber as described in Chapter-2. The temperature of the photocatalytic chamber was 306 K.

#### 6.4.3.1 Photocatalytic enhancement of Nip reduction with glycerol

The reaction mixture with the catalyst (S8 or S9) was prepared as given in section 3.2.2.2.This was then irradiated by visible light from cool white LED source (approximately 940 watts/$m^2$) in the photocatalytic chamber at 306 K. The absorption spectrum of the reaction mixture was recorded after every 10 minutes time interval.

### 6.4.3.2 Photocatalytic oxidation of methyl orange dye

The reaction mixture with the catalyst was prepared as given in section 3.2.2.3. The reaction mixture was kept in the photocatalytic chamber at 306 K and then irradiated by visible light from cool white LED source (approximately 940 watts/$m^2$). The photocatalytic activities were measured for S8 and S9 Ag-Cu BNPs catalysts samples in this manner.

## 6.4.4 Results and discussion

### 6.4.4.1 Characterization of Ag-Cu BNPs

X-ray diffraction patterns of the nanoparticle powder samples S8 and S9 BNPs are shown in Figure 6.4.1. Both S8 and S9 BNPs samples show five peaks at 2θ = 38.18°, 44.40°, 64.66°, 77.07° and 81.25° corresponding to the {111}, {200}, {220}, {311} and {222} planes of FCC silver.

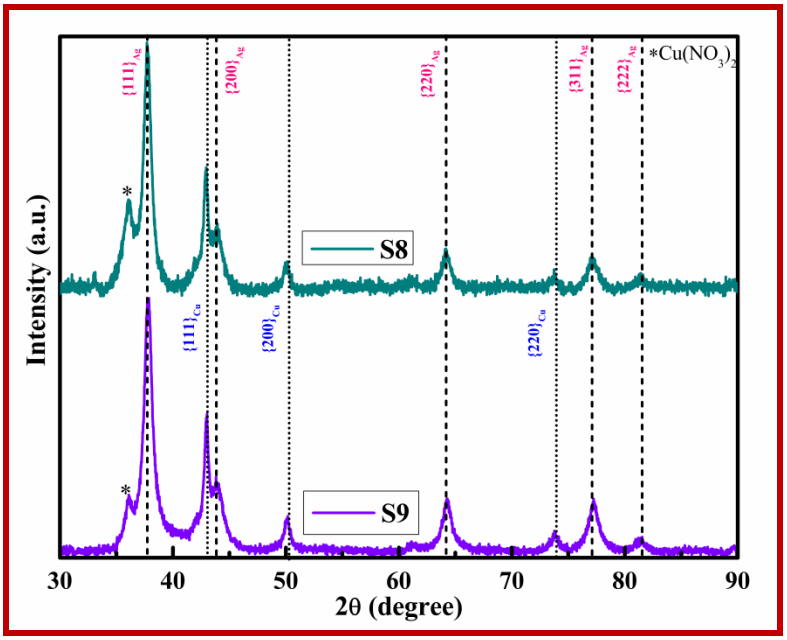


**Figure 6.4.1** X-ray powder diffraction patterns of S8 and S9 Ag-Cu BNPs samples.

Moreover, three peaks at 43.22°, 51.06° and 74.16° corresponding to {111}, {200} and {220} planes of FCC copper are also observed. Thus, XRD analysis confirms the formation of both pure FCC Ag and FCC Cu phases in both S8 and S9. In the XRD pattern of both S8 and S9, there are peaks marked by * at 34.53°. This peak corresponds to the unreduced precursor copper nitrate salt.

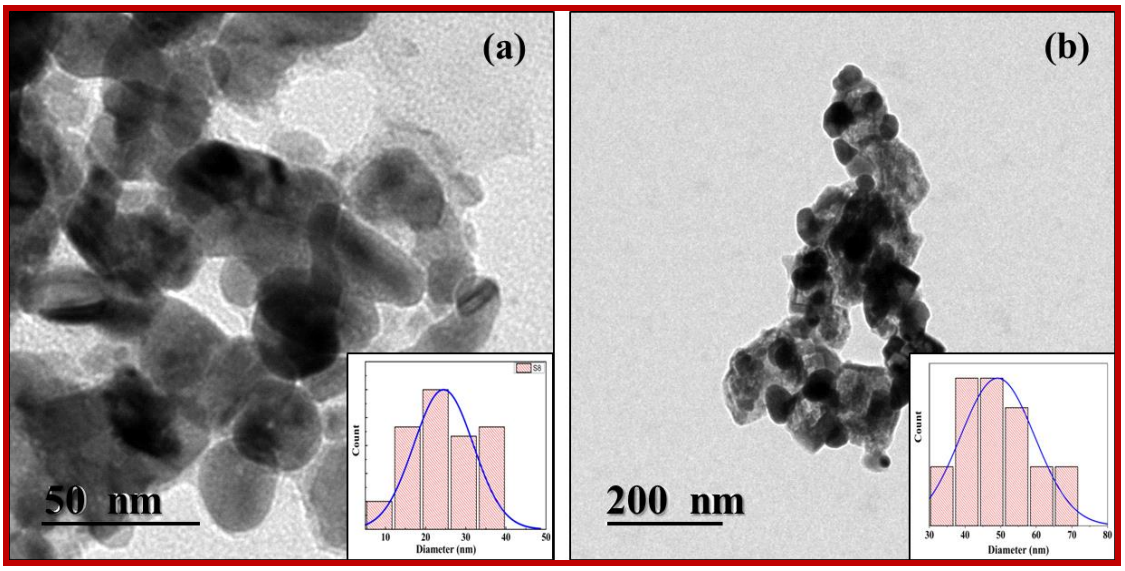


**Figure 6.4.2** TEM micrograph of Ag-Cu BNPs, S8 **2 (a)** and S9 **2 (b)** samples. The corresponding particle size histogram is shown in inset of each TEM micrograph.

The TEM micrographs of S8 and S9 BNPs samples are shown in Figure 6.4.2. The images show that the particles are almost spherical in shape in both the samples. The average particle sizes for S8 and S9 BNPs are found to be ~ 25 and ~ 50 nm respectively from the particle size distribution histograms.

Further, HR-SEM imaging was carried out to record the elemental mapping of Ag and Cu components present in both S8 and S9 samples (Figure 6.4.3). Phase separated

domains of Ag and Cu can be seen clearly in the elemental mapping images. Since the nanoparticles are quite fine, therefore, the distribution of phase-separated domains in individual nanoparticles is heterogeneous. Furthermore, only few (phase separated) Ag rich and Cu rich domains make up individual BNPs nanoparticles.

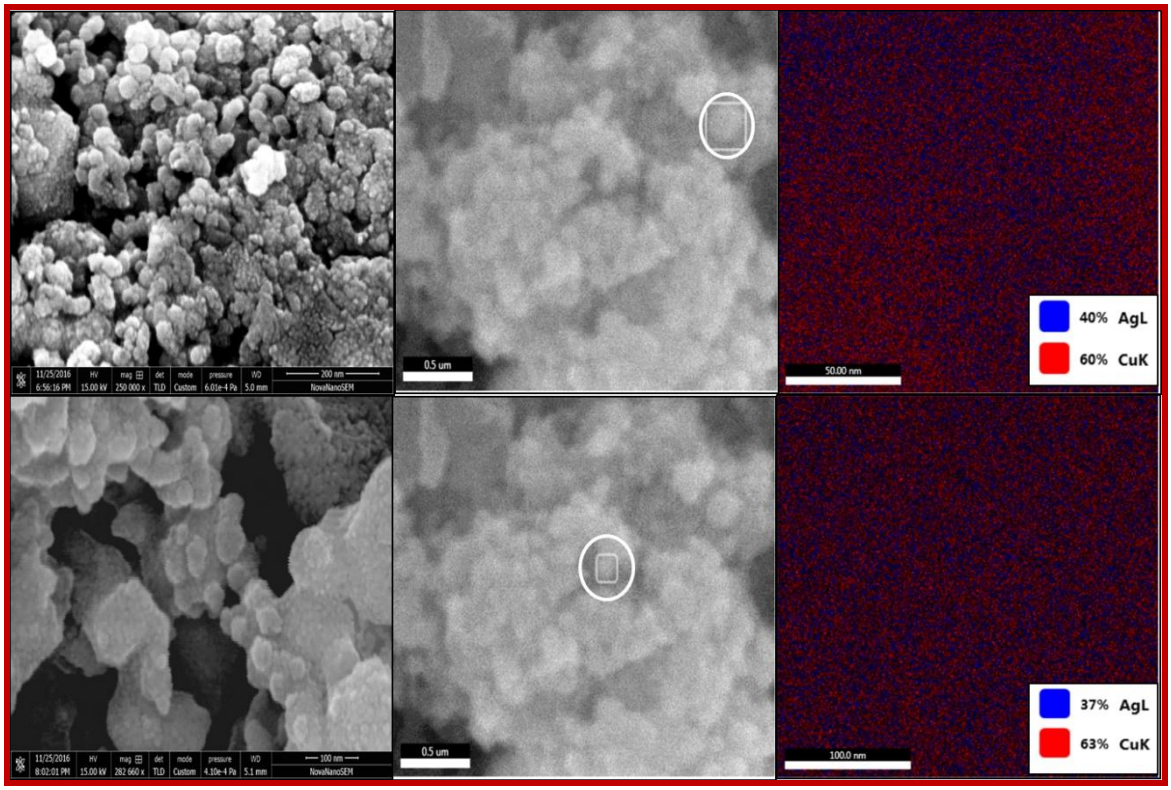


**Figure 6.4.3** HR-SEM images of S8 and S9 Ag-Cu BNPs samples **3 (a), 3 (b)** and corresponding elemental mapping of particles **3 (e), 3 (f)** respectively. Particle on which mapping was done is shown in the inset of corresponding SEM image **3 (c), 3 (d).**

The UV-visible spectra of S8 and S9 Ag-Cu BNPs sol samples are shown in Figure 6.4.4. Two LSPR absorbance maximums at ~ 402 and ~ 578nm can be seen in the UV-visible spectrum of aqueous suspension of S8. Sample S9 shows absorbance maximums at ~ 399 and ~ 583 nm. Thus, the UV-visible spectra of both the BNPs show the presence of Ag and Cu LSPR. This indicates the presence of Ag-rich and Cu-rich BNPs. Besides this, it can also

be seen that the UV-visible spectrums (for both S8 and S9) display relatively high absorbance intensities at wavelengths which are between the LSPR maximums for pure AgNPs and CuNPs. This suggests the presence of bimetallics of intermediate compositions or presence of both Ag and Cu domains in individual BNPs.

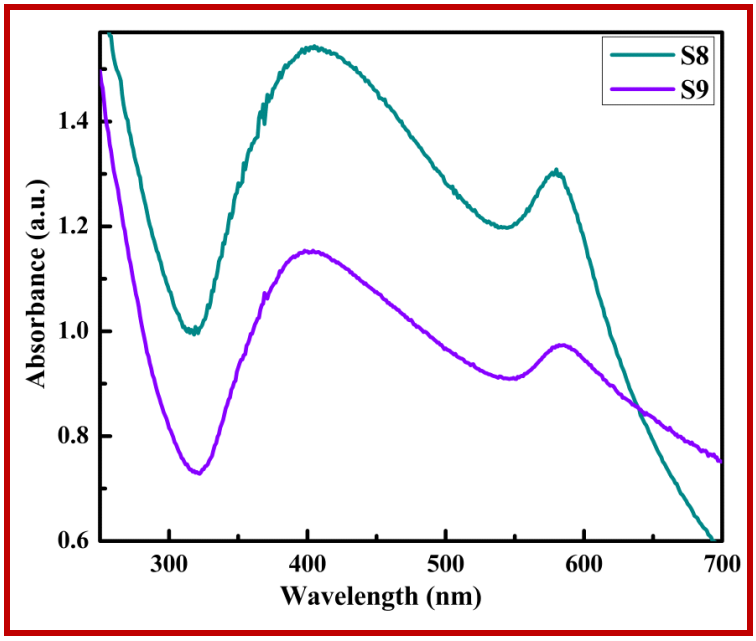


**Figure 6.4.4** The UV-Vis absorbance spectra of aqueous dispersion of S8 & S9 BNPs sol samples.

### 6.4.4.2 Catalytic Nip reduction with $NaBH_4$ and Gly

The UV-spectra giving the Nip reduction by $NaBH_4$ in presence of S8 catalyst is displayed in Figure 6.4.5 (a). The spectrum shows decrease in intensity of absorption peak at ~ 400 nm for *p*-nitrophenolate ions with time. Simultaneously, a smaller absorbance maximum at ~ 301 nm is gradually seen to increase with time. This was due to the formation of the reaction product AP. Also, the spectrum shows two isosbestic points at ~ 283 and ~

312 nm which indicate that Nip fully converts to AP without any side reaction [Kaur *et al*. (2016)].

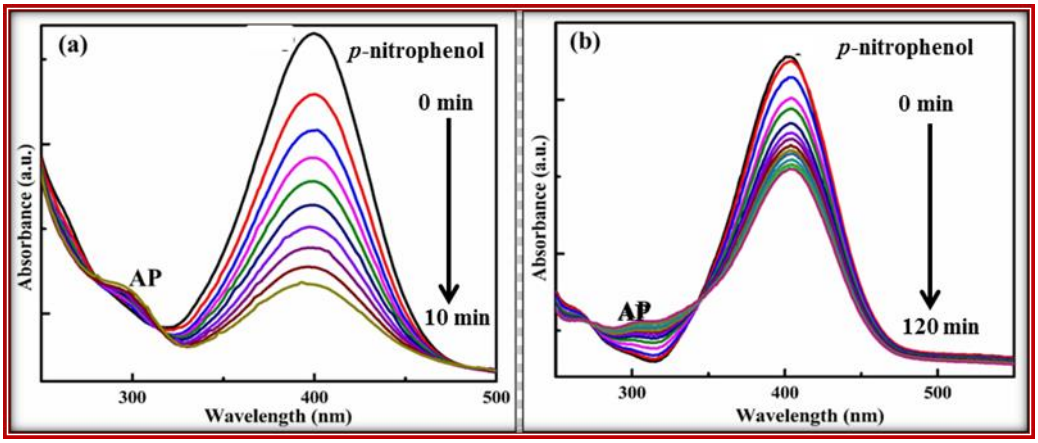


**Figure 6.4.5** UV-Vis absorption spectra for *p*-nitrophenol reduction by $NaBH_4$ **5 (a)**, UV-vis absorbance of *p*-nitrophenol reduction by glycerol versus time in presence of S8 BNPs catalyst **5 (b)**.

The time evolution of the UV-visible spectrum for Nip reduction by Gly in presence of S8 catalyst is shown in Figure 6.4.5 (b). The absorbance maximum of *p*-nitrophenolate at ~ 406 nm is seen to decrease with time. Concurrently, the absorbance at ~ 306 nm increases due to formation of AP. Since the isosbestic points are not very clear, therefore, the product was further confirmed by a preliminary qualitative analysis and then $^1$HNMR was carried out to identify the actual product formed. The preliminary identification of presence of aromatic amine functional group was done by the azo dye test [Vogel (1978)]. This test resulted in the formation of orange colored azo dye which indicates the formation of *p*-aminophenol. Afterwards, $^1$HNMR of the product was carried out in DMSO solvent (Figure 6.3.6). The $^1$HNMR spectrum gives peaks at δ 8.35 (s, 2 H), 7.27 – 5.02 (m, 4 H), 4.38 (s, 2 H). These are in agreement with three types of hydrogens (H) present in AP. This confirms the formation of AP in the product. These tests for identification of the product were done for

reaction carried out in presence of S9 BNPs as well. In this case also, Nip reduction by Gly result in the same AP product formation.

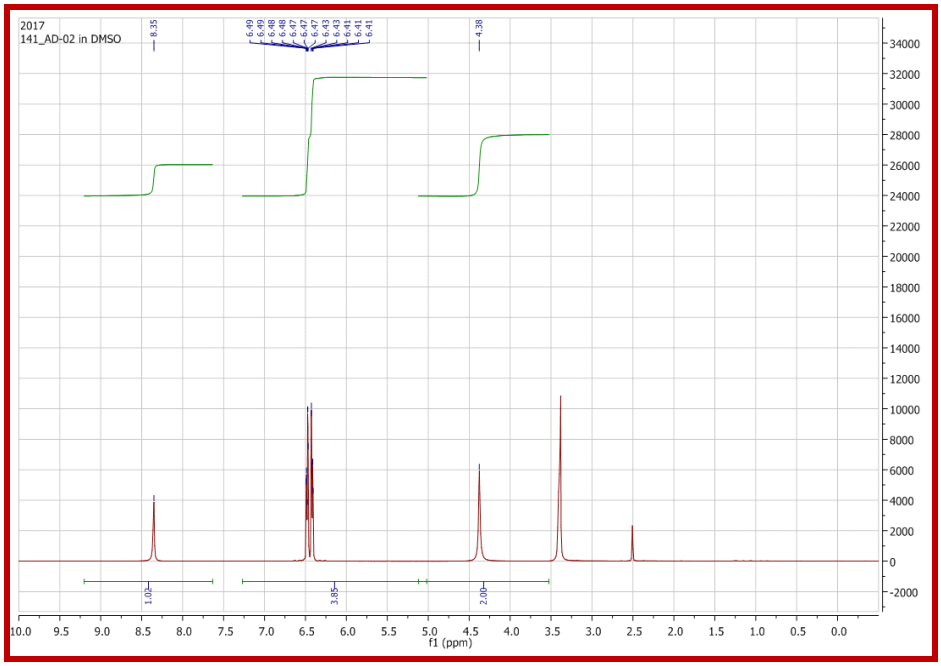


**Figure 6.4.6** NMR spectrum of product of Nip reduction with glycerol in presence of S8 BNPs.

**Reduction kinetics**

The reducing agent ($NaBH_4$) was taken in large excess (~ 40 times) as compared to Nip concentration. Therefore, the concentration of the reductant remained almost constant during the reaction. The order with respect to Nip, determined using Eqn. 3.3 for its reduction by $NaBH_4$, follows pseudo first order kinetics for both S8 and S9 BNPs catalyst. In keeping with this, a $\ln(A/A_0)$ versus time plot is plotted in Figure 6.4.7 (a). This plot shows that initially there was a time gap (the induction time $t_{ind}$) during which no reduction took place. Thereafter, a nice linear fit to the plot, in accordance with pseudo first-order kinetics, was obtained. The slope of this fit gives rate constants.

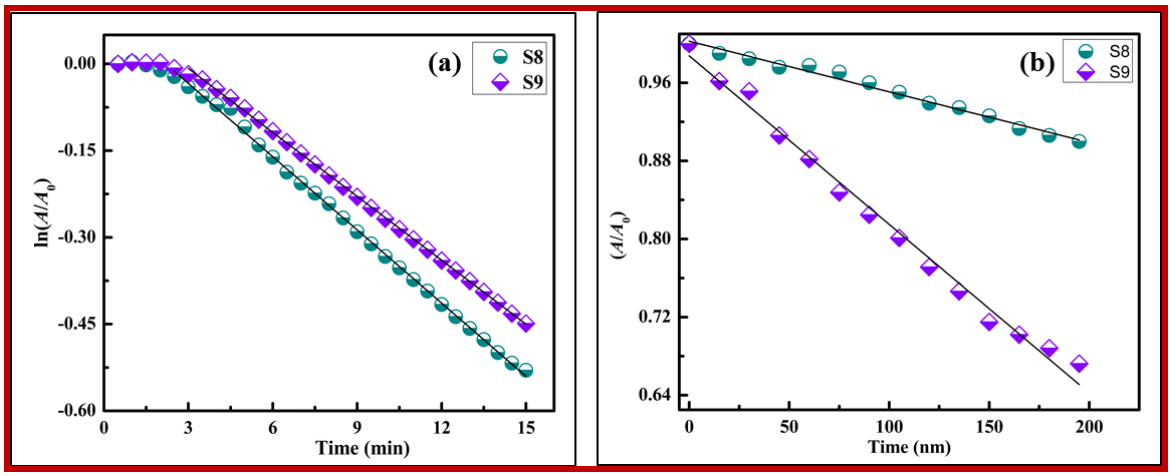


**Figure 6.4.7** Variation of ln($A/A_0$) [absorbance ($A$) measured at ~ 401 nm] Vs time with $NaBH_4$ reductant **7 (a)**. Variation of $A/A_0$ [absorbance ($A$) measured at ~ 406 nm] Vs time with Gly as reductant in presence of both S8 and S9 BNPs catalyst **7 (b)**. The $R^2$ value of all the fittings is ~ 0.98.

The value of n when Nip is reduced with Gly is found to be 0, which suggest this reduction follows zero order kinetics with respect to Nip for both S8 and S9 BNPs catalyst. Therefore, the plot between $A/A_0$ and time gives a linear fit with respect to both S8 and S9 (Figure 6.4.7 (b)). No induction time could be observed in this case. As mentioned earlier, this is possibly due to low solubility of oxygen in glycerol [Kutsche *et al.* (1984)]. The slope of the linear fit to this plot is used to obtain the $k_{app}$ value.

The $k_{app}$ and TOF values for Nip reduction by $NaBH_4$ or Gly are tabulated in Table 6.4.1. Besides this, the Table also gives the BNPs size and respective activation energies. To calculate the activation energies, this reduction reaction was carried out at four different temperatures. The slope of the linear fit to ln($k_{app}$) versus 1/$T$ plots was used to calculate the activation energies as per the linearized Arrhenius equation [Eqn. 3.4 in Chapter-3] (Figure 6.4.8).

**Table 6.4.1** Average particle size, apparent reaction rate constants and activation energy for Nip reduction with $NaBH_4$ and Gly as reducing agent in presence of both S8 and S9 BNPs catalyst.

| Catalyst | Particle size D (nm) | Apparent reaction rate constant ($k_{app}$) | | Activation energy ($E_a$) (kJ/mol) | | TOF ($min^{-1}$) | |
|---|---|---|---|---|---|---|---|
| | | $NaBH_4$ ($min^{-1}$) | Gly (mol $lit^{-1}min^{-1}$) | $NaBH_4$ | Gly | $NaBH_4$ | Gly |
| **S8** | ~ 25 | 0.0421 | 0.0005 | ~ 68.1 | ~ 90.2 | ~ 112 | ~ 5.7 |
| **S9** | ~ 50 | 0.0368 | 0.0017 | ~ 61.2 | ~ 54.1 | ~ 125 | ~ 7.7 |

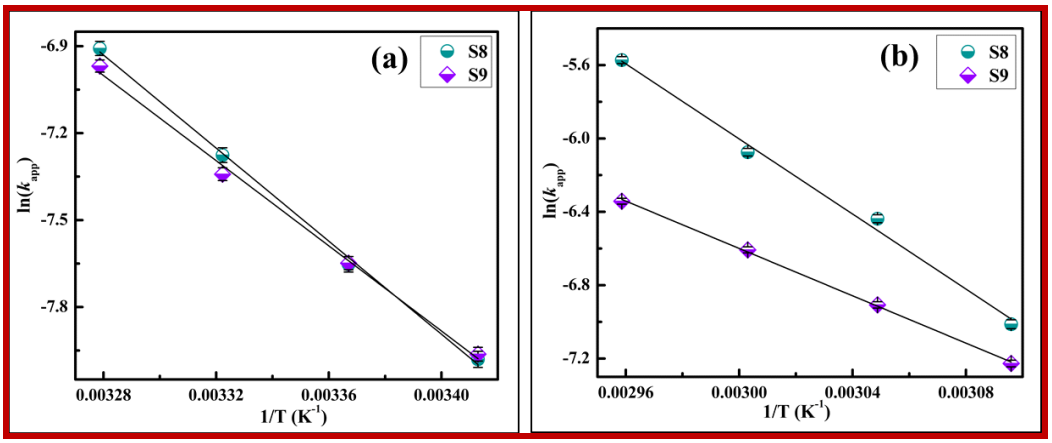


**Figure 6.4.8** Arrhenius plot for Nip reduction reaction catalyzed by S8 and S9 BNPs samples with reducing agents $NaBH_4$ **8 (a)** and Gly **8 (b).** Error bars are very small in most of the cases. The $R^2$ value of all the fittings is ~ 0.98.

In case of Nip reduction by $NaBH_4$, the $k_{app}$ value for S8 is higher than that of S9. However, there is not much difference between $k_{app}$ values obtained for S8 and S9. The activation energies found are also comparable. The slightly higher $k_{app}$ value for S8 can therefore be attributed to smaller average particle size.

For Nip reduction by Gly, $k_{app}$ value found for S9 is about three times that of S8. This is despite the difference between the average particle sizes of S8 and S9. In view of this, it can be assumed that the higher catalytic activity of S9 is due to the lower activation energy for reaction catalyzed by S9 than when catalyzed by S8 BNPs.

#### 6.4.4.3 Photocatalytic study

For photocatalytic reduction by Gly in presence of S8 or S9, the order with respect to Nip was found to be 0. Since the order with respect to Nip follows zero order kinetics for both thermal and photocatalytic conditions, therefore it appears that the basic mechanism of Nip reduction by Gly remains the same even when it is carried out under visible light irradiation. The slope of this linear fit of the plot between $A/A_0$ and time gives $k_{app}$ values for Nip reduction with Gly (Figure 6.4.9). These $k_{app}$ values are tabulated in Table 6.4.2. As in the thermally catalyzed case, here also S9 exhibits higher photocatalytic activity than S8. Moreover, both S8 and S9 exhibit significant photocatalytic enhancement when the reaction is carried out under visible light of cool white LED's. Hence, plasmonic excitation of electrons occurs for both catalysts. Additionally, altering of electronic states (and thereby the transition between them) due to adsorption of Nip on the surface of such plasmonic BNPs, could also facilitate vibrational energy gain by the adsorbate through photon absorption induced vibronic energy exchange as per Frank-Condon principle.

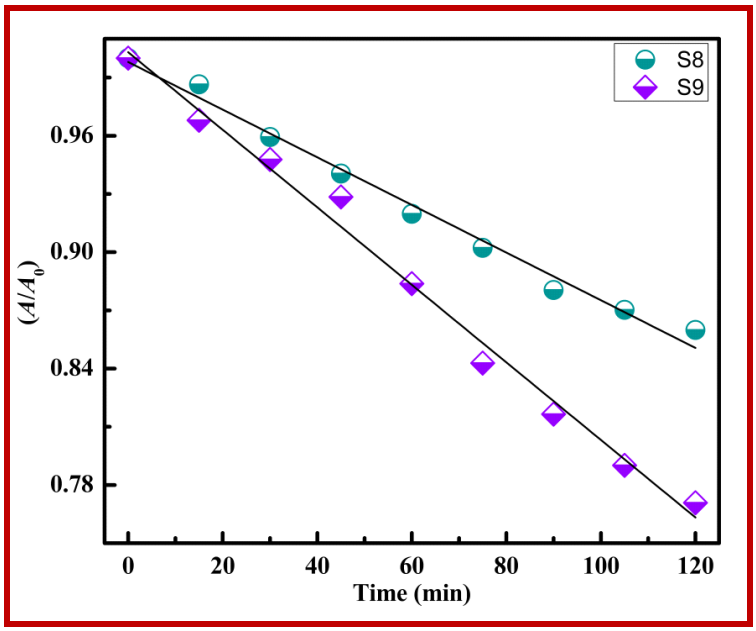


**Figure 6.4.9** Variation of $A/A_0$ [absorbance ($A$) measured at ~ 406 nm] versus time in photocatalytic Nip reduction with Gly. The $R^2$ value of all the fittings is ~ 0.98

**Table 6.4.2 D**isplays the photocatalytic apparent reaction rate constant, photocatalytic turn over frequency (PTOF) and TOF for Nip reduction with Gly as reducing agent at 306 K.

| Catalyst | Photocatalytic apparent reaction rate constant ($k_{app}$) (mol lit$^{-1}$min$^{-1}$) | Turn over frequency (min$^{-1}$) | |
|---|---|---|---|
| | | TOF | PTOF |
| **S8** | 0.0012 | ~ 5.7 | ~ 10.5 |
| **S9** | 0.002 | ~ 7.7 | ~ 13.9 |

### 6.4.4.4 Methyl orange oxidation thermal and photocatalytic

Figure 6.4.10 displays the change in UV-visible spectrum for oxidative degradation of MO with time. All three initial peaks present in the UV-visible spectrum of MO in acidic medium undergo degradation with progress of time. No new absorption peak could be observed in the UV-visible spectrum during the oxidative degradation. As per the mechanism proposed in Figure 3.16 (Chapter-3) for oxidative degradation of MO, if the degradation had

stopped at either stage (A, B) or C or D, then the MO degradation UV-visible spectra would have shown the emergence of a new peak. However, as mentioned earlier, no such peak could be observed in either Figure 3.11 (b) or 3.11 (c). This indicates that the MO must have been degraded at least till stage (E, F, G).

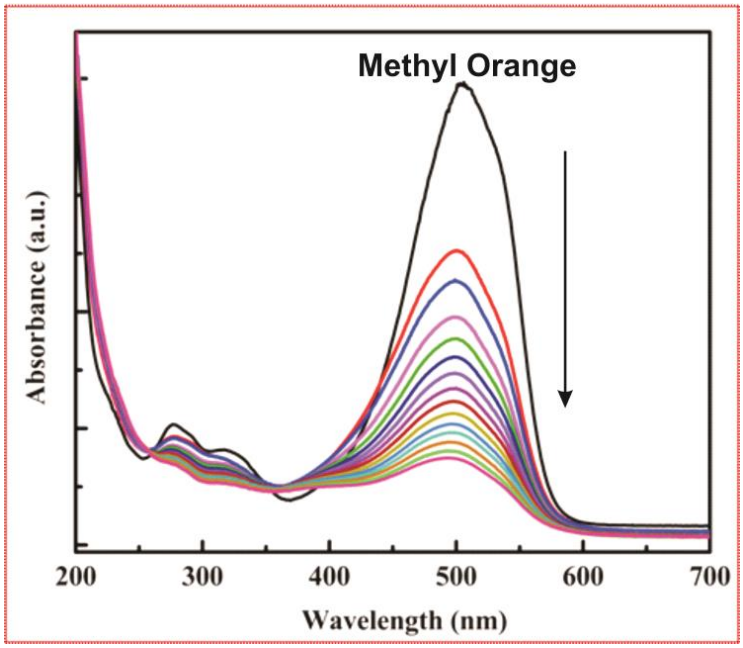


**Figure 6.4.10** Variation of absorbance maximum of MO (~ 506 nm) with $H_2O_2$ oxidizing agent in presence of catalyst S8 BNPs catalyst.

The order n for MO degradation, obtained by the procedure discussed in Chapter-3 [Eqn.3.3], is 2. The order is same for both thermally and photocatalytically catalyzed MO degradations (using both S8 and S9 BNPs). Consequently, the respective $k_{app}$ values are found from the slopes of the linear fits for the plots between $1/A_t$ versus time for thermal and photocatalytic MO degradations (Figure 6.4.11). The thermal and photocatalytic apparent reaction rate constants associated with oxidative MO degradation in presence of BNPs

catalyst are summarized in Table 6.4.3. Further, this degradation was studied at different temperatures to calculate the activation energies by utilizing the linearized Arrhenius equation given in Chapter-3 [Eqn.3.4]. The plot between ln($k_{app}$) verses 1/T gives a linear plot and the slope (-$E_a$/R) of this plot gives activation energy (Figure 6.4.12). The $E_a$ values for thermal MO degradation in presence of these catalysts are mentioned in table 6.4.3.

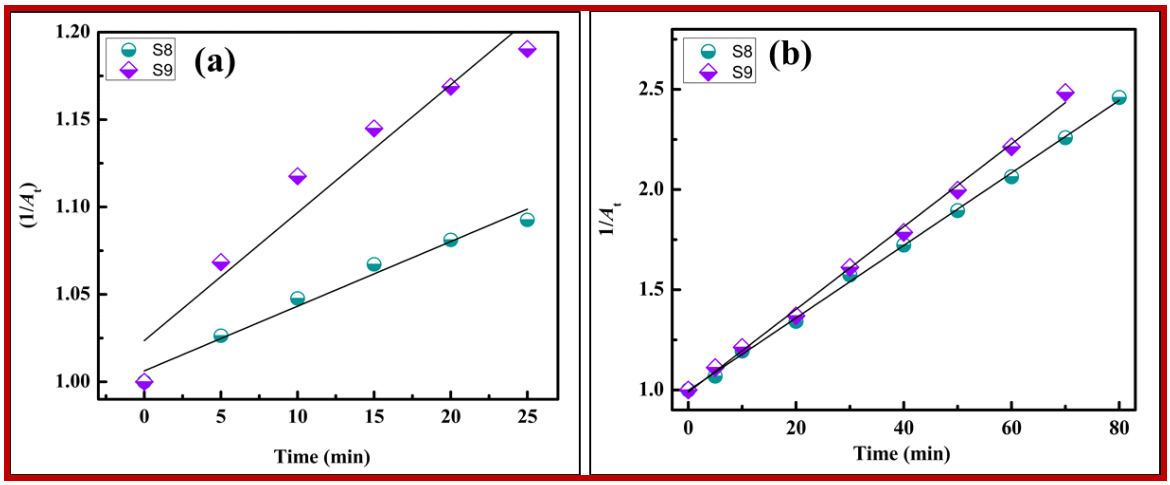


**Figure 6.4.11** Variation of ($1/A_t$) [absorbance ($A$) measured at ~ 506 nm] Vs time thermal **11 (a)**. and photocatalytic **11 (b)** MO degradation in presence of both S8 and S9 BNPs catalyst. The $R^2$ value of all the fittings is ~ 0.96.

For thermally catalyzed MO degradation, the $k_{app}$ and TOF values obtained for S9 are higher than those for S8 BNPs catalyst. The activation energy, when the reaction was catalyzed by S9, is almost half of that which was found when the reaction was carried out in presence of S8 BNPs. Since the average BNPs size of S8 is smaller than S9, therefore, it is likely that the higher catalytic activity associated with S9 is primarily owing to the lower activation energy value for this reaction.

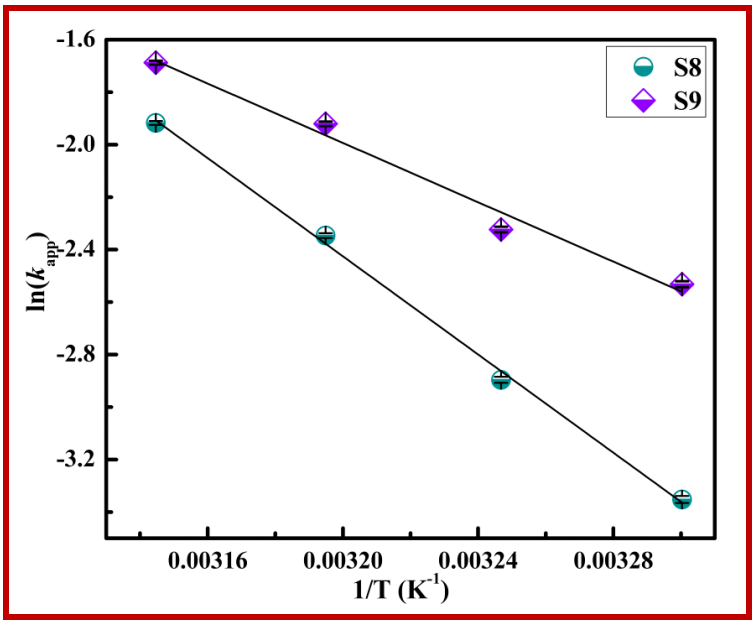


**Figure 6.4.12** Arrhenius plot for MO degradation catalyzed by S8 and S9 BNPs samples. Error bars are very small in most cases. The $R^2$ value of all the fittings is ~ 0.98.

**Table 6.4.3** Apparent reaction rate constant, activation energy and turnover frequency (TOF) for thermal and photocatalytic MO degradation at 306 K in presence of both S8 and S9 BNPs catalyst.

| **Catalyst** | **Apparent reaction rate ($k_{app}$) ($mol^{-1}$ lit $min^{-1}$)** | | **Activation energy ($E_a$) (kJ/mol)** | **Turn over frequency ($min^{-1}$)** | |
|---|---|---|---|---|---|
| | **Thermal** | **Photo** | | **TOF** | **PTOF** |
| **S8** | 0.0037 | 0.019 | ~ 78.2 | ~ 1.6 | ~ 2.9 |
| **S9** | 0.0072 | 0.021 | ~ 42.1 | ~ 2.2 | ~ 3.1 |

In contrast to this, for visible light photo Fenton degradation of MO, the $k_{app}$ and PTOF values are nearly the same for the reaction photocatalyzed by either S8 or S9. Since the order of the reaction is same, whether MO degradation is carried out thermally or photocatalytically, therefore, possibly the reaction mechanism is the same in both cases. In

this case, the visible light photocatalytic enhancement is more for S8. Thus, resulting in almost doubling of the catalytic activity when the reaction is carried out in presence of light. However, the enhancement is not that much when the reaction is photocatalyzed by S9. Higher plasmonic photocatalytic enhancement observed for MO degradation catalyzed by S8 BNPs, could be because of its smaller size and hence larger surface area.

### 6.4.5 Conclusions

This chapter dealt with the preparation and catalytic properties of three different types of PVP stabilized Ag-Cu bimetallic nanoparticles (BNPs). The first type of Ag-Cu bimetallics nanostructures were prepared by a polyol method. Bimetallic nanoparticles, phase-separated into very fine/small Ag-rich and Cu-rich domains, were obtained. The average BNPs size being large (~ 100 nm), quite a few of such domains exist on individual nanoparticles. Because of this, the samples with different Ag : Cu precursor salt ratio's display only one LSPR maximum absorbance. Furthermore, the LSPR maximum shifts with the precursor Ag : Cu ratio. In fact, an almost linear relation between the LSPR maximum and the precursor Ag : Cu composition is obtained. Anisotropic shapes are also observed in TEM images of samples consisting of Ag : Cu ratio of 1 : 1 and 2 : 1.

There is synergistic increase in catalytic activity when Ag : Cu ratio is 1 : 1 whether Nip is reduced by $NaBH_4$ or glycerol. This is because of higher density of phase boundaries in individual BNPs that give rise to more number of catalytically active sites. After this composition, the TOF values for $NaBH_4$ reduced Nip reaction decreases with increase in Ag component (S3, S4 and S5) in the bimetallic nanoparticles. This appears to be consequence of a combination of increase in activation energies and induction times as Ag component increases in Ag-Cu BNPs.

Nip reduction by glycerol follows second order kinetics (with respect to Nip). This is in contrast to the first order kinetics observed when the reduction is by $NaBH_4$. The TOF values of Nip reduction by glycerol also show maximum synergistic catalytic activity at 1 : 1 Ag : Cu ratio and it decreases as one progresses from sample S2 to S4. However, in this case the activation energy values decrease with increase in Ag component (from S2 to S4) in bimetallic catalyst. It appears that the number of active sites for glycerol reduction of Nip on the bimetallic nanoparticles decreases from S2 to S4. Catalytic sites due to anisotropic shapes in S2 and to some extent in S3 may be contributing to this effect.

On carrying out Nip reduction by Gly in visible light, surprisingly the catalytic activity decreases. The decrease, relative to the thermal activity, is maximum for 1 : 1 (or S2) Ag : Cu ratio. On increasing the ratio of Ag (S3 and S4), the decrease in catalytic activity due to exposure to visible light, becomes lesser. It appears that the plasmonic excitation of electrons is quenched by the neighboring Cu surface patch. The lesser the amount of Cu on the surface, lesser is the quenching and thereby as the amount of Cu decreases the difference in catalytic activity of thermal and photocatalytic activities.

The oxidative (Fenton like) MO degradation catalyzed by these BNPs also showed synergistic catalytic activity at 1:1 Ag: Cu ratio (S2). Significant photocatalytic enhancement (50-70 %) could be observed for S2 and S4 BNPs samples. But in S3, slight decrease in MO degradation catalytic activity in presence of light is observed. The synergistic catalytic activity exhibited by S2 could be because, at 1 : 1 precursor ratio, there are more Ag-Cu phase boundaries that give rise to catalytically active sites with the lowest activation energy.

The second type of BNPs prepared by polyol techniques are two core-shell nanostructures viz. Ag shell Cu core (S6) and Cu shell Ag core (S7). The core shell systems

S6 and S7 BNPs synthesized by polyol protocols have almost similar average particle sizes. Nanoparticles in S6 have roughly spherical shapes. On the other hand, doughnut shaped nanostructures are also observed in S7. In view of such doughnut shaped nanostructures, the average surface area for nanostructures of S7 is definitely more. However, the core shell S6 BNPs catalyst shows better catalytic activity (than S7) for Nip reduction by Gly, as well as for oxidative degradation of MO. In Nip reduction with $NaBH_4$ it got reversed. Here, activation energy as well as higher surface area favored better catalytic activity of S7 BNPs catalyst in Nip reduction with $NaBH_4$. However, for both reactions (Nip reduction with Gly and MO degradation) shows higher photocatalytic enhancement with S6 BNPs catalyst. It appears that the Ag shell of S6 BNPs has higher density of catalytically active centres for these reactions. Since the shell is thin, therefore, the Cu core harvested visible light photons are able to channel that energy into the catalytically active centres on the nanostructure shell.

Finer sized Ag-Cu BNPs were obtained when the reduction was carried out by alkaline hydrazine hydrate. The synthesis was carried out by co-precipitating Ag and Cu on precursor Cu seeds. The Ag-Cu phase separated BNPs samples of two different sizes are obtained by changing the Ag to Cu salt precursor ratios. These BNPs have comparatively smaller sizes than those prepared in EG. Given their preparation protocol and finer sizes, the much smaller number of separate Ag domains and Cu domains exist in individual BNPs. Furthermore, the distribution of such phase separated domains is also heterogeneous. S8 BNPs catalyst shows better Nip reduction with $NaBH_4$ compared to S9 BNPs owing to smaller average particle size and high surface area. On the other hand, S9 BNPs demonstrates better catalytic activity for Nip reduction (with Gly) and MO degradation. Significant visible light photocatalytic activity enhancement occurs when Nip reduction (with Gly) and MO

degradation are catalyzed by either S8 or S9. However, the trend of catalytic activity remains the same as in absence of light. That is, S9 has better photocatalytic activity than S8. This is an important finding, since S9 consists of Cu rich BNPs.

Overall, among the three types of BNPs investigated in this chapter, the catalytic and photocatalytic activities of the core-shell bimetallic nanoparticles (particularly Ag shell and Cu core), are found to be the best.